

MIT Open Access Articles

Dynamics of circular arrangements of vorticity in two dimensions

The MIT Faculty has made this article openly available. **Please share** how this access benefits you. Your story matters.

Citation: Swaminathan, Rohith V. et al. "Dynamics of Circular Arrangements of Vorticity in Two Dimensions." *Physical Review E* 94, 013105 (July 2016): 1-19 © 2016 American Physical Society

As Published: <http://dx.doi.org/10.1103/PhysRevE.94.013105>

Publisher: American Physical Society

Persistent URL: <http://hdl.handle.net/1721.1/110274>

Version: Final published version: final published article, as it appeared in a journal, conference proceedings, or other formally published context

Terms of Use: Article is made available in accordance with the publisher's policy and may be subject to US copyright law. Please refer to the publisher's site for terms of use.



Dynamics of circular arrangements of vorticity in two dimensions

Rohith V. Swaminathan,¹ S. Ravichandran,² Prasad Perlekar,² and Rama Govindarajan^{2,*}

¹*MIT/WHOI Joint Program in Oceanography, Massachusetts Institute of Technology, Cambridge, Massachusetts 02139, USA*

²*TIFR Centre for Interdisciplinary Sciences, Tata Institute of Fundamental Research, Hyderabad 500075, India*

(Received 20 October 2015; revised manuscript received 13 June 2016; published 7 July 2016)

The merger of two like-signed vortices is a well-studied problem, but in a turbulent flow, we may often have more than two like-signed vortices interacting. We study the merger of three or more identical corotating vortices initially arranged on the vertices of a regular polygon. At low to moderate Reynolds numbers, we find an additional stage in the merger process, absent in the merger of two vortices, where an annular vortical structure is formed and is long lived. Vortex merger is slowed down significantly due to this. Such annular vortices are known at far higher Reynolds numbers in studies of tropical cyclones, which have been noticed to break down into individual vortices. In the preannular stage, vortical structures in a viscous flow are found here to tilt and realign in a manner similar to the inviscid case, but the pronounced filaments visible in the latter are practically absent in the former. Five or fewer vortices initially elongate radially, and then reorient their long axis closer to the azimuthal direction so as to form an annulus. With six or more vortices, the initial alignment is already azimuthal. Interestingly at higher Reynolds numbers, the merger of an odd number of vortices is found to proceed very differently from that of an even number. The former process is rapid and chaotic whereas the latter proceeds more slowly via pairing events. The annular vortex takes the form of a generalized Lamb-Oseen vortex (GLO), and diffuses inward until it forms a standard Lamb-Oseen vortex. For lower Reynolds number, the numerical (fully nonlinear) evolution of the GLO vortex follows exactly the analytical evolution until merger. At higher Reynolds numbers, the annulus goes through instabilities whose nonlinear stages show a pronounced difference between even and odd mode disturbances. Here again, the odd mode causes an early collapse of the annulus via decaying turbulence into a single central vortex, whereas the even mode disturbance causes a more orderly progression into a single vortex. Results from linear stability analysis agree with the nonlinear simulations, and predict the frequencies of the most unstable modes better than they predict the growth rates. It is hoped that the present findings, that multiple vortex merger is qualitatively different from the merger of two vortices, will motivate studies on how multiple vortex interactions affect the inverse cascade in two-dimensional turbulence.

DOI: [10.1103/PhysRevE.94.013105](https://doi.org/10.1103/PhysRevE.94.013105)

I. INTRODUCTION

Vortices may be considered to be fundamental building blocks of turbulent flows. The study of collections of point vortices has been found to be useful in understanding two-dimensional turbulence [1]. Merger events are believed to be of central importance in the inverse cascade of turbulent kinetic energy in two-dimensional turbulence [2–4]. In a turbulent flow dense with vorticity, the most common form of interaction is between two vortices, but it is not unusual for three or more vortices to interact. While the merger process of two identical vortices is extremely well studied (see, e.g., Refs. [5] and [6]), in this paper, we investigate the merger and breakup of several vortices and the breakup of an annulus of vortex.

We study a model flow consisting of several (up to nine) equal like-signed vortices placed initially on the vertices of regular polygons, and find that the merger of $N > 2$ vortices shows several features distinct from the two-vortex case. The summary of our findings is depicted schematically in Fig. 1. Vortex merger depends on both whether the number of vortices is odd or even, and on the Reynolds number of the flow. At relatively low Reynolds number, we find an annular vortex stage in the merger process. This annular structure remains axisymmetric but reduces in radius to eventually produce a single merged Lamb-Oseen vortex. On the other hand the

evolution at high Reynolds numbers is more complicated. An annular vortex loses symmetry and the flow becomes turbulent as it decays. The vortices in a system of an even number of vortices, e.g., 6 or 8, pair up to form a four-vortex configuration which then undergoes further mergers. More fascinating is the case of the merger of an odd number of vortices. Here, all vortices cannot pair and the merger process is more turbulent. The system rapidly degenerates into decaying turbulence. Our system possesses of course many more degrees of symmetry than are likely to occur too often in turbulent flow. A more general initial condition would not have identical vortices exactly on the vertices of regular polygons. However annular structures that break up into vortices are seen in real atmospheric flows (e.g., [7]). A regular structure such as ours reduces the number of variables to be specified as a first step.

We also numerically investigate the stability of an annular vortex. This problem was first studied by [8], who performed inviscid stability analysis and numerical simulations with broadband initial perturbations and found a ring of elevated vorticity perturbed with azimuthally broad-banded initial conditions to go unstable and form multiple vortices, which undergo further rearrangement to a near monopolar circular vortex. We study how the wave number of the initial perturbation affects the stability of the annular vortex, and find similar growth rates for the $m = 4$ mode as Schubert *et al.* [8].

At low Reynolds number the annular vortex is stable and peak vorticity decays via diffusion. However at higher Reynolds number the annular vortex becomes unstable. The

*rama@tifrh.res.in

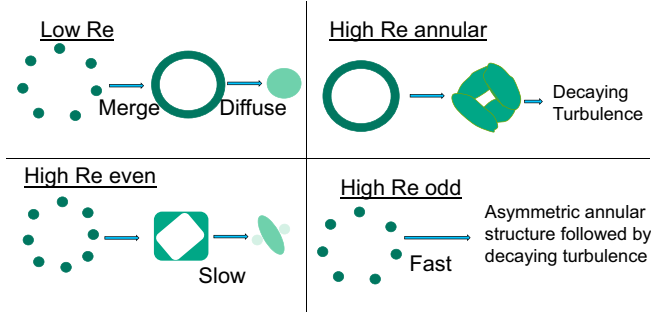


FIG. 1. A schematic summarizing the dynamics. At low Reynolds number, n corotating vortices will merge to form an annular structure, which then diffuses inwards to form a single Lamb-Oseen vortex. At high Reynolds number, an annular vortex is not stable. It breaks into several vortices, and creates decaying turbulence. n vortices at high Reynolds number will form an annuluslike structure which is symmetric when n is even and asymmetric when n is odd. The former will decay into a tripolar structure while the latter will break down quickly into decaying turbulence.

linear growth rate is positive for a range of azimuthal wave number, and the variation with wave number is smooth. In the nonlinear stages of disturbance growth, however, we see some interesting behavior. Similar to vortex merger at high Reynolds number, the nonlinear destabilization of the annular vortex strongly depends on whether the initial perturbation is even or odd. This final stage of the merger process is similar to what happens in inviscid flow, where a thin annulus often goes unstable and bunches up into several patches of vorticity.

We first examine what is known about the inviscid case because it provides a comparison and contrast with the viscous study to follow.

II. DYNAMICS OF MULTIPLE VORTICES IN INVISCID FLOW

Consider an inviscid system with n corotating point vortices, each of circulation Γ/n , and separated by a distance $d/2$ from the centroid of the system, as shown in Fig. 2. These vortices are confined by the Biot-Savart law to motion

on a circle of diameter d , with an azimuthal velocity of $u_\theta = (n-1)\Gamma/(n\pi d)$. In a coordinate frame rotating with the same angular velocity as the vortices, the system is in steady state, with the positions of the vortices, as well as the streamlines, frozen. There are several saddle points in this frame of reference, and the vortices themselves act as centers. Streamlines connecting the saddle points, either homoclinically or heteroclinically, form separatrices in the flow, as shown in Figs. 2(a) and 2(b) for two and six vortices respectively. The separatrices divide the fluid flow into distinct regions: (1) central, (2) inner core, (3) exchange band, (4) outer recirculating, and (5) external flow [9]. Regions 2 comprise the immediate proximity of the vortices, so the vortex dominates the motion and closed streamlines are seen. In regions 4, too, flow follows closed streamlines in the rotating coordinate system, and the fixed points (not shown) within these are centers. The outer recirculating region has fluid rotating in a sense opposite to the inner core and exchange band regions. Only region 2 contains vorticity. The central region exists only when we have three or more vortices; this is evident in Figs. 2(b) and 2(c). The exchange band is seen to be a thin band of fluid, which will be seen to become important in filament formation. It is well known in the two-vortex viscous case to be of importance during the merger process; we will see how it affects the dynamics in the multiple-vortex case.

The point vortex system was shown long ago [10,11] to be unstable for $n > 7$. Among the host of studies that followed, we pick our way through only the most relevant for the present work. Primary among these is Dritschel [9] who extended the work of Thomson to the case of n finite patches of uniform vorticity rather than point vortices, placed initially at the vertices of a regular polygon, and allowed to undergo inviscid dynamics. If the vortices have finite but small radius a , such that (a/d) is much less than a critical ratio $(a/d)_{\text{crit}}$, the dynamics is similar to that of point vortices. Larger inviscid patches do not remain circular but their shapes may be obtained exactly. If $(a/d) \geq (a/d)_{\text{crit}}$, the vortices, while rotating around each other, deform and also move towards each other, but Kelvin's circulation theorem prevents any reconnection of their boundaries. In the case of vortices with finite size, nonlinear inviscid studies [12] so far

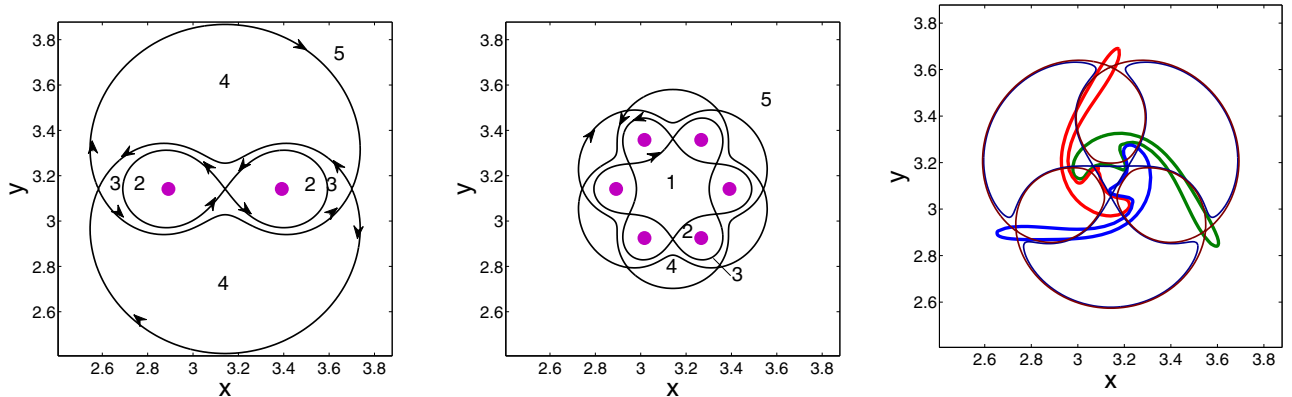


FIG. 2. Separating streamlines in the corotating frame for two (left) and six (center) point vortices. The vortices are indicated by large (pink online) dots. The regions are distinguished as follows: (1) central (not present for two vortices), (2) inner core, (3) exchange band, (4) outer recirculating and (5) external flow. Right: Separatrices for three point vortices (thin lines) overlaid on three patches of uniform vorticity which evolved starting from circular patches at the same positions as the point vortices (solid lines).

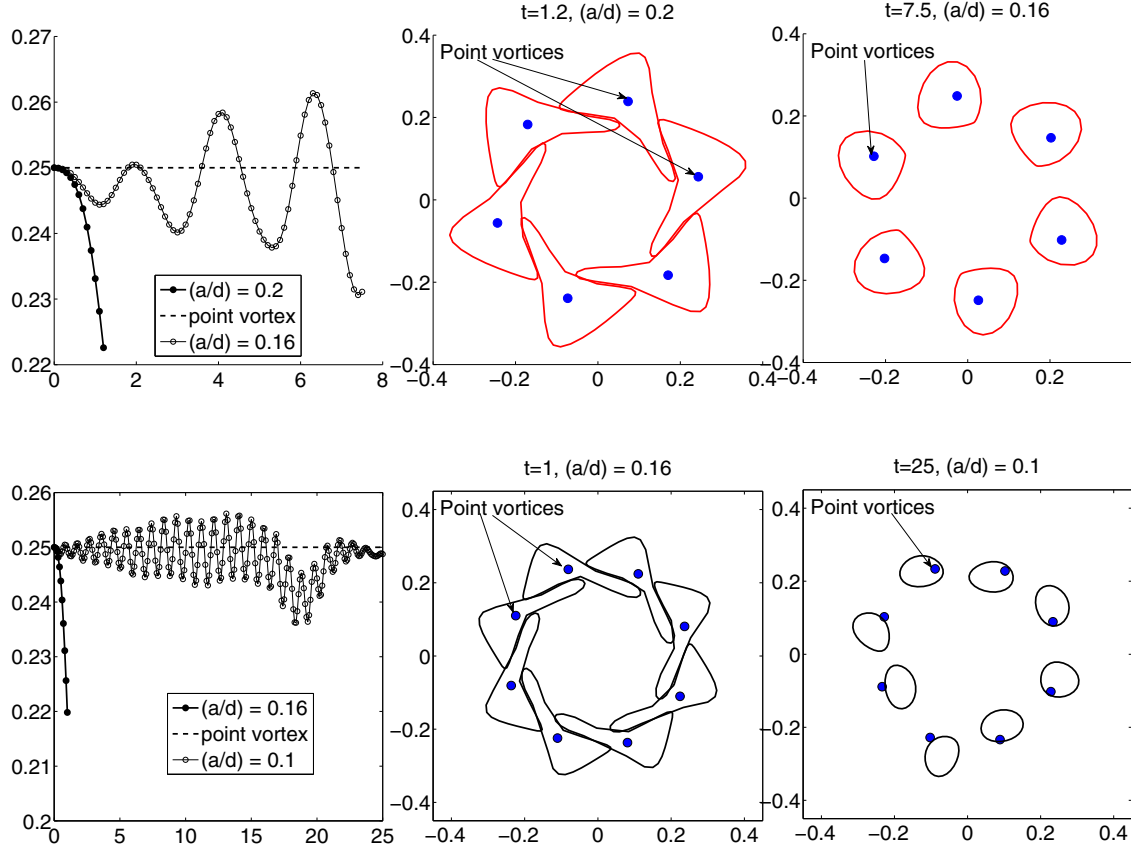


FIG. 3. Inviscid simulations of vortex patches with $(a/d)_i > (a/d)_{\text{crit}}$ and $(a/d)_i < (a/d)_{\text{crit}}$ for $N = 6$ (top) and $N = 8$ (bottom). The average radial distance of the patches from the origin is shown on the left panels. For $N = 6$, the $(a/d)_{\text{crit}}$ is higher than the value for $N = 8$. It is seen that the dynamics up to the time shown, in terms of the radial location, is similar to that of the point vortices when the patches are far apart from each other at the initial time. Also the shape deviates from the circular, but remains convex. Note however that eight patches which start $(a/d)_i < (a/d)_{\text{crit}}$ go unstable and therefore do not remain axisymmetric, whereas the point vortices occupy (by the analytical expressions) the vertices of a rotating octagon at all times. When the initial separation is smaller, the patches for $N = 6$ as well as for $N = 8$ undergo rapid changes in shape, and the average distance from the center decreases rapidly.

have indicated that these vortices collapse into an annuluslike structure.

To differentiate finite size effects from viscous diffusion effects, we start with circular patches of uniform vorticity, rather than point vortices, placed at the vertices of regular polygons, and allow their shapes to evolve inviscidly. The inviscid patch vorticity simulations have been carried out using a contour dynamics code from Pozrikidis [13]. Figure 2(c) shows how vortex patches have evolved in a three-vortex configuration. An annular vortical structure is formed surrounding a small central region without vorticity. The patches have developed long tails as well. Separatrices of the point vortex configuration are shown in the same figure for comparison. It is seen that the central region is the same for both patch and point vortices.

Figure 3 shows how an annular structure forms for $N = 6$ and $N = 8$ patches. For small initial patch radii a_i , the vortex patches are strained from their initially circular shapes, but remain separate. The left panels of the figures show that the vortex centers oscillate about their initial radial distance with a systematic increase in amplitude in the six-vortex case and chaotically in the eight-vortex case. On the other hand, for $(a/d)_i > (a/d)_{\text{crit}}$, the patches reorient themselves azimuthally and undergo a distinct change in shape. The long

tails of the patches are seen to be folded inwards for $N = 6$ and $N = 8$, unlike at $N = 3$ where they were pointed outwards. It may be inferred from Fig. 3 that $(a/d)_{\text{crit}}$ is between 0.16 and 0.2 for $N = 8$, and between 0.1 and 0.16 for $N = 6$; i.e., $(a/d)_{\text{crit}}$ decreases with increasing N . When the patches are too close or the filaments too thin, inviscid simulations become prohibitively expensive.

An inviscid annular vortex on the other hand goes unstable to azimuthal disturbances and splits into smaller multiple vortices [12]. Symmetric neutral disturbances of large azimuthal wave number are the only ones that resist instability.

III. SIMULATIONS OF VORTEX MERGER

A. Numerical scheme and initial conditions

Since the flow is incompressible and two dimensional, we may work with the vorticity and stream function equations:

$$\frac{\partial \omega}{\partial t} + \frac{\partial \psi}{\partial y} \frac{\partial \omega}{\partial x} - \frac{\partial \psi}{\partial x} \frac{\partial \omega}{\partial y} = \nu \nabla^2 \omega, \quad (1)$$

$$\nabla^2 \psi = -\omega, \quad (2)$$

where ω and ψ are the vorticity and stream function respectively, x and y are spatial coordinates, and t is time. We solve this system by a Fourier pseudospectral technique [14,15] for spatial discretization, with standard de-aliasing using the 2/3 rule. Simulations at high Reynolds numbers and those for the stability of an annular vortex structure are time evolved with an exponential Adams-Bashforth temporal discretization. Unless stated otherwise, we work with a square domain of area $4\pi^2$ and discretize it with N^2 collocation points with $N = 2048$.

At the initial time, n identical corotating vortices (n varying from 2 to 8) are arranged at equal intervals on the circumference of a circle of radius R , i.e., on the vertices of a regular polygon. Each of these vortices has a Gaussian initial vorticity profile given by $\omega = \omega_0 e^{-r^2/a^2}$, with a total circulation in the system given by Γ . Here r is the radial location measured from the center of each vortex. In our simulations, unless explicitly mentioned otherwise, we prescribe $(a/d)_i = 0.1$ at $t = 0$, where the subscript i refers to initial conditions. To make fair comparisons between cases of different n , we follow two approaches. In the first case, we keep the total initial circulation Γ constant across the set of simulations. The Reynolds number is then given by

$$\text{Re}_\Gamma = \frac{\Gamma}{\nu}, \quad (3)$$

and the time scale is the period of rotation of point vortices of the same strength, given by

$$T_\Gamma = \frac{2n\pi^2 d^2}{(n-1)\Gamma}. \quad (4)$$

In the following, wherever we refer to Re without a subscript, we mean Re_Γ .

In the second case, we keep the total initial energy, within a domain of diameter d_0 , constant across the set of simulations. The Reynolds number is based on the root mean square velocity u_{rms} within this domain, and its size:

$$\text{Re}_E = \frac{u_{\text{rms}} d_0}{\nu}, \quad (5)$$

with the time scale $T_E = d_0/u_{\text{rms}}$.

In viscous flow, two vortices which come close enough to touch each other merge into one vortex. This process has been described in great detail; see, e.g., Refs. [5,6,16–19]. If the initial radius of each vortex is much smaller than the distance separating their centers, the vortices rotate at a constant frequency as described above. Simultaneously they grow in size by viscous diffusion. Once their radius reaches a critical fraction ($= 0.22$) of their separation distance, enough vorticity has entrained into the exchange band, which creates filamentary structures that induce a radially inward velocity on the vortices, bringing them close to each other. This is followed by a second diffusive stage where the separation decreases slowly to 0, whence an axisymmetrization of the merged vortex follows. The filamentary debris is erased by viscosity during this time. A typical history of the separation distance is shown in Fig. 4 which also serves as a validation of our numerical approach.

All the results presented here use an initial separation $d_i = 0.5$ for the vortices. This initial separation is chosen so that the

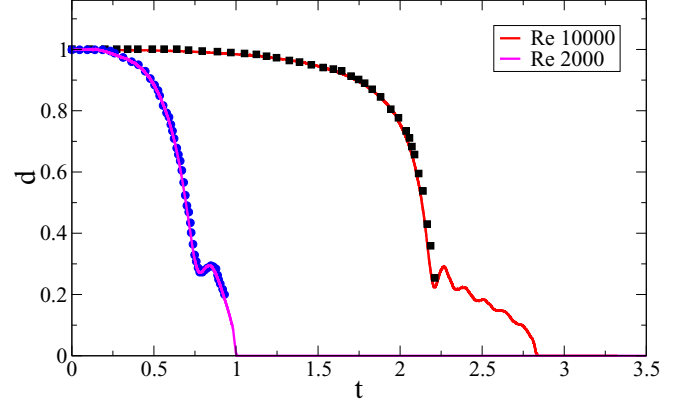


FIG. 4. Evolution of the separation distance in the merger of two identical vortices. The results of Ref. [20] ($\text{Re} = 2000$, blue filled circles) and Ref. [21] ($\text{Re} = 10000$, black filled squares) compared to present simulations.

vortices are all well within the periodic box, and image effects are minimized. We verify this by performing simulations with boxes of size $\pi \times \pi$ and $4\pi \times 4\pi$ the present size. Representative results are shown in Fig. 5. In the six-vortex case, symmetry breaks by two adjacent vortices merging, and the corresponding pair diametrically opposite doing the same. Numerical noise decides which among the adjacent vortices will merge. Changing the domain size changes this choice in this case, so an apparent change in orientation is seen in the merged structures. Apart from this there are minor differences in detail. We note that the flow system we study has a net vorticity, whereas by applying periodic boundary conditions we force the induced velocity to zero at the boundaries. This does produce small numerical errors.

We also verify that the effects of using a Cartesian grid on an axisymmetric problem are negligible, as follows. Two initial conditions rotated relative to each other by an angle of $\pi/5$ are simulated. The results are compared in Fig. 6, which shows that the energies in the two simulations are identical until the very end. Again the symmetry breaking occurs due to numerical noise, and decides which pair of vortices merge. In Fig. 7, therefore, (counting from the top) vortices 2 and 3 and 5 and 6 merge first in the simulation on the left, whereas on the right, vortices 1 and 2 and 4 and 5 merge first. This leads to merged structures that appear to be rotated by more than $\pi/5$.

To contrast later with multiple-vortex merger, we present in Fig. 8 the viscous evolution of two Gaussian vortices. Notice the tilt of the vortices with respect to the radial direction at intermediate times, and the filaments in the outer region. The tilt of the vortices plays an important role in merger, and leads, as we will see below, to vortices merging azimuthally, instead of radially.

B. Merger of multiple vortices at moderate Reynolds number

To show why three or more vortices are different from two, we return to Fig. 2. The annular nature of the exchange band region and the consequent existence of a central passive

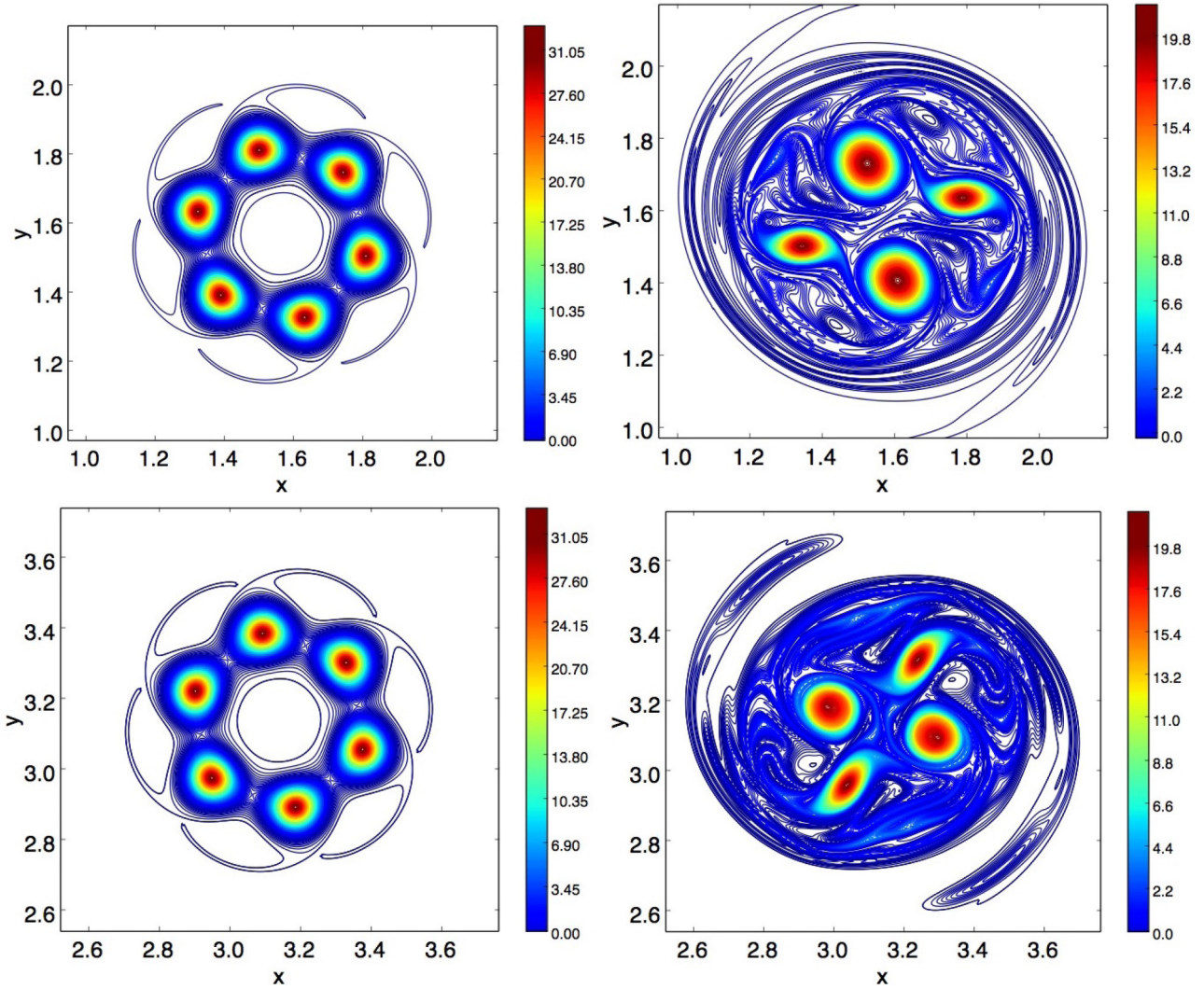


FIG. 5. Contour plots of the vorticity field for a box of size π^2 (top row) and $4\pi^2$ (bottom row) at times $t = 4.6$ (left) and $t = 14.86$ (right). We see that main vortex structures are very similar. However, because of the large-scale counter vortex being different in the two cases, the details of the vortex wings are different.

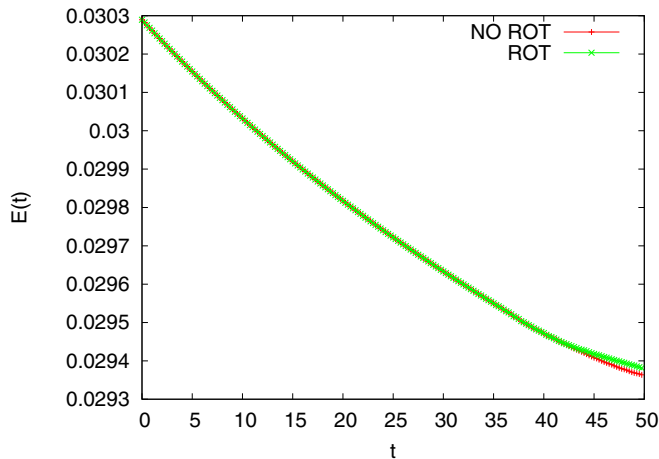


FIG. 6. The energy in two simulations rotated by $\pi/5$ relative to each other. The energies are identical until the very end of the simulations where numerical noise becomes important and makes the two curves diverge.

region means that for $n \geq 3$ vortices tend to align azimuthally rather than radially. The formation of an azimuthally restrained vortical structure is evident in Fig. 2(c). Such a structure will be contrasted with an axisymmetric annulus formed in viscous merger. In addition, we point out that although the merger of multiple vortices is fundamentally no different from the merger of two vortices, the well-known sequence of events in two-vortex merger is not followed and is replaced, instead, by the formation of the annulus and a much slower relaxation to a single vortex at the origin.

Four-vortex merger is shown in Fig. 9, where the initial (a/d) is chosen such that merger will occur. Patch vortices are shown superimposed on the separatrices. The initial convective stage of the dynamics is seen to be similar in the inviscid and viscous cases. However, the realignment and shape are different at later stages, and sharper filaments of exchange-band vorticity are seen. In particular, the tails of the vortex patches in the inviscid case are shrunk and blunted in the viscous case. The central vorticity-free region is seen

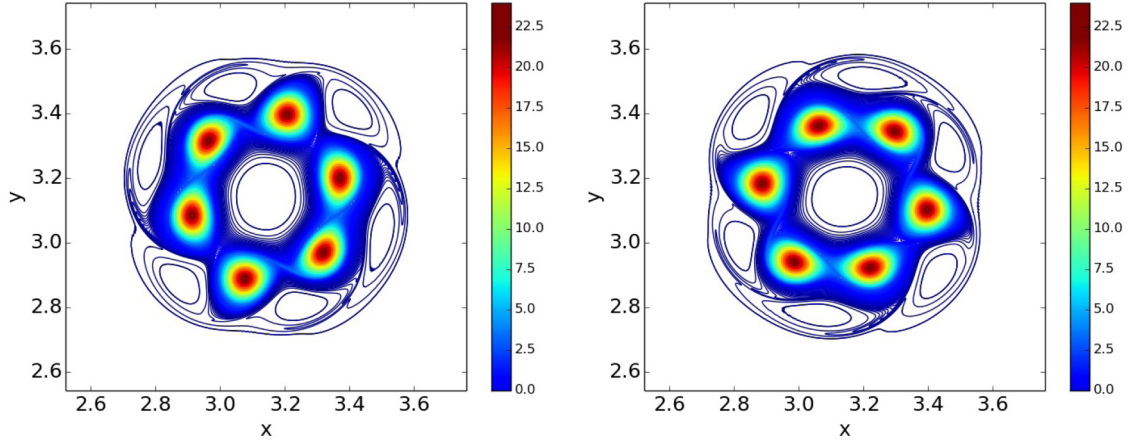


FIG. 7. Vorticity contours for the simulations from Fig. 6 at time = 35. The figure on the right was started with the vortices rotated by $\pi/5$ relative to the vortices in the left figure. Note that the angle between the figures is now closer to $\pi/2$. See text for an explanation.

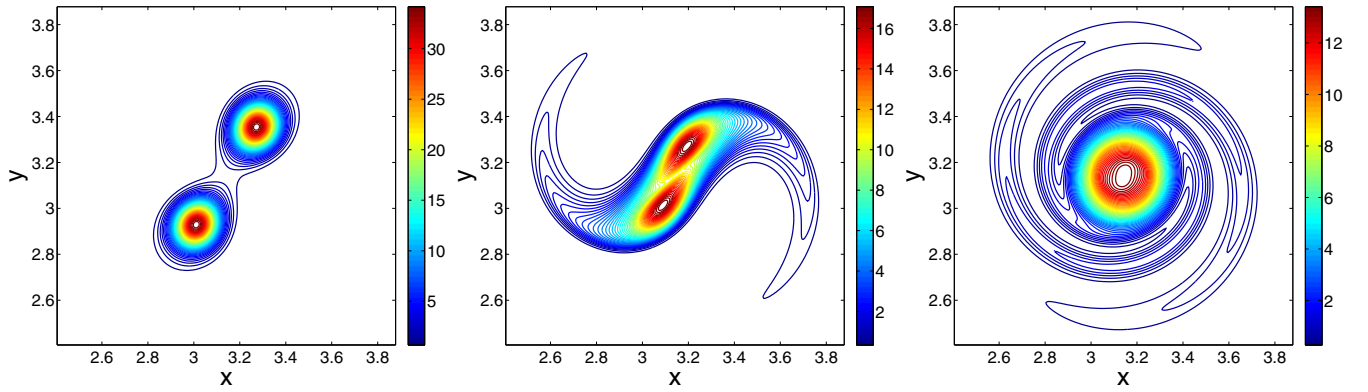


FIG. 8. Vorticity contours showing the viscous evolution of two Gaussian vortices with $(a/d)_i = 0.1$ and $\text{Re}_\Gamma = 4000$. Left: $t = 0.669$; center: $t = 1.52$; right: $t = 2$.

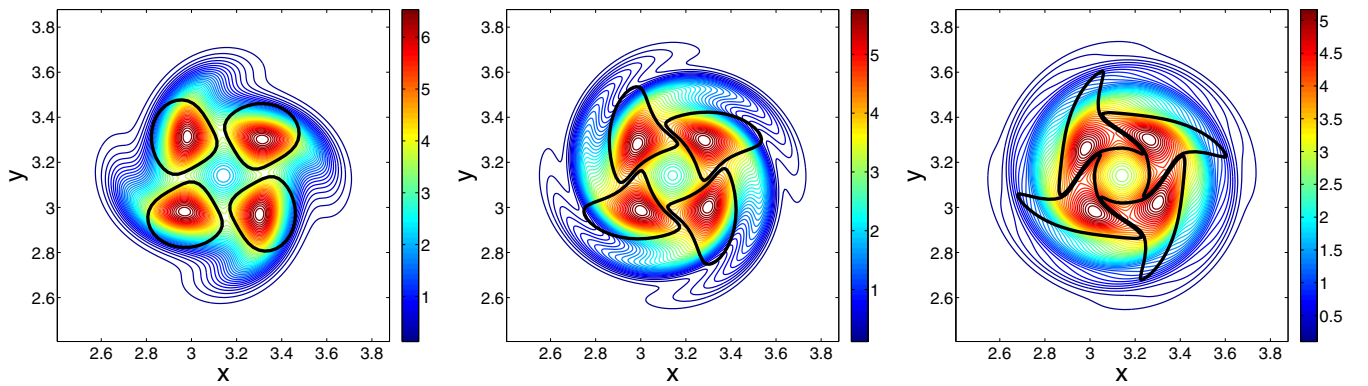


FIG. 9. Vorticity contours showing the viscous evolution of four Gaussian vortices with $(a/d)_i = 0.3$ and $\text{Re}_\Gamma = 4000$. A gentle initial radial alignment is seen. Left: $t = 0.81$; center: $t = 2.43$; right: $t = 4.86$. The solid black lines show the inviscid evolution of patches of vortices of uniform vorticity (and the same total strength) at the corresponding times.

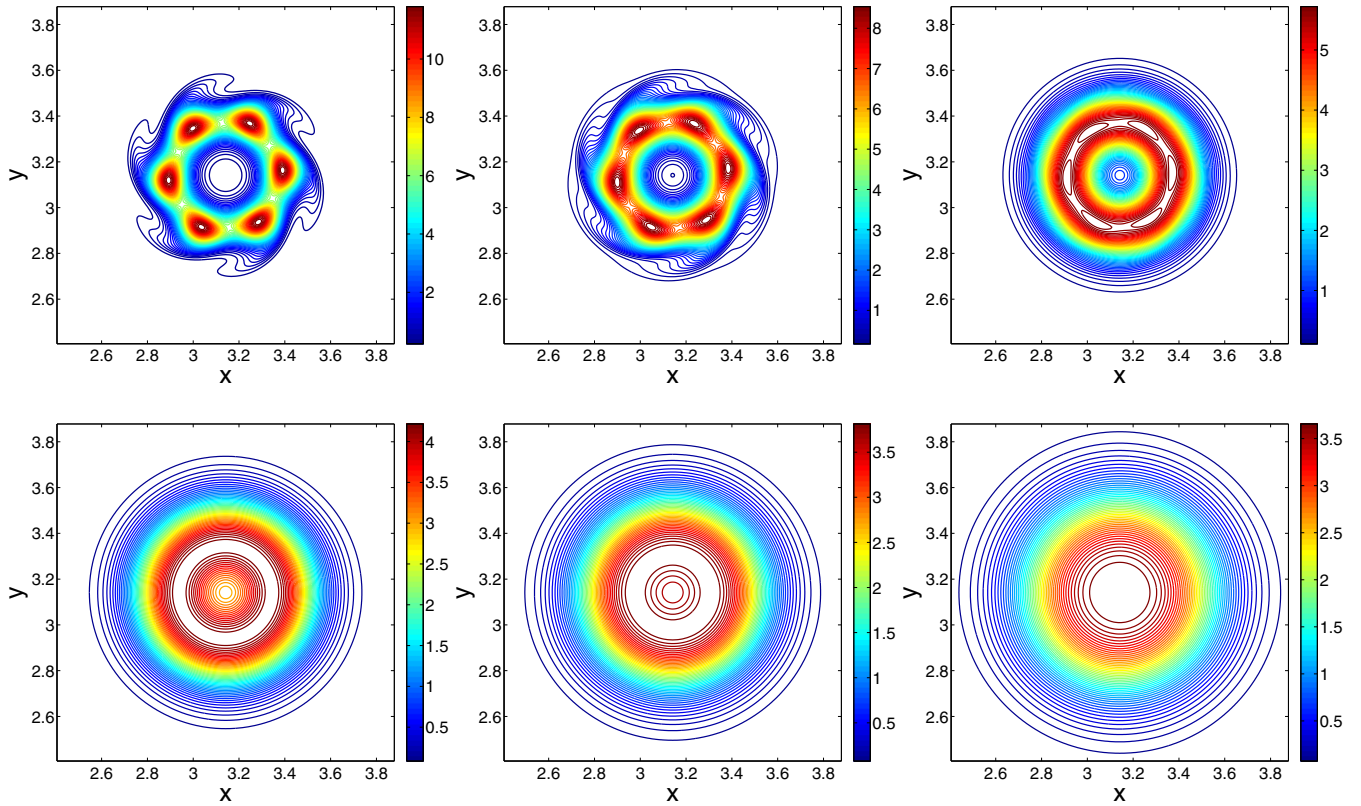


FIG. 10. Vorticity contours showing the viscous evolution of six Gaussian vortices with $(a/d)_i = 0.1$ and $\text{Re}_\Gamma = 4000$. Observe initial azimuthal alignment, very clean annulus, and the subsequent inward motion of the annulus to form a single maximum. Times shown (left to right, top row): $t = 1, t = 1.52, t = 2.7$; bottom row: $t = 5.4, t = 7.5, t = 10.47$.

to be affecting the dynamics in a passive manner, effecting an azimuthal realignment, and in the viscous case, giving rise at later times to an axisymmetric annular structure (not shown). The case of three vortices is not shown for brevity, but it proceeds in a manner very familiar to the four-vortex case. Figure 10 shows the viscous evolution of six Gaussian vortices. The strain field now is such that even at short times, the vortices align themselves azimuthally, forming an axisymmetric annulus. Note that such axisymmetry is

impossible in inviscid evolution. There is then a slow reduction in radius of the annulus on a diffusive time scale, to finally form a single Gaussian vortex. The formation of filaments is minimal, unlike in the merger of two vortices. To summarize, merger is now an azimuthal phenomenon, like people on a dance floor joining hands to form a circle, and does not result immediately in the formation of a vorticity maximum at the center. The latter is attained on a diffusive time scale.

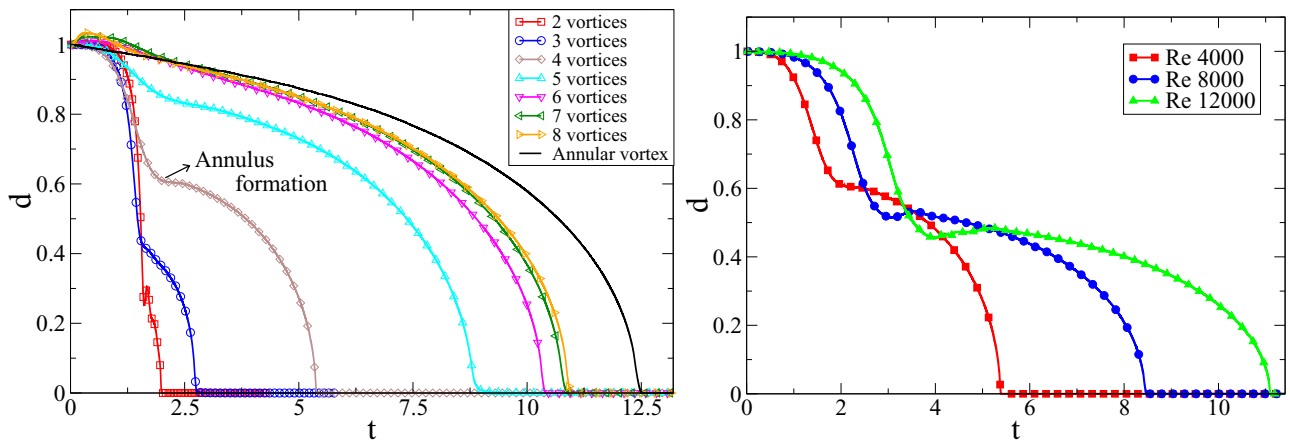


FIG. 11. Left: Nondimensional separation distance d (scaled by the initial separation) as a function of the nondimensional time t at $\text{Re}_\Gamma = 4000$. The curves shift to the right as the number increases. Starting with six or more vortices is qualitatively the same as starting with a pure annular vortex. Here $(a/d)_i = 0.1$. Right: Separation distance d vs time t for four vortices, for different Re_Γ .

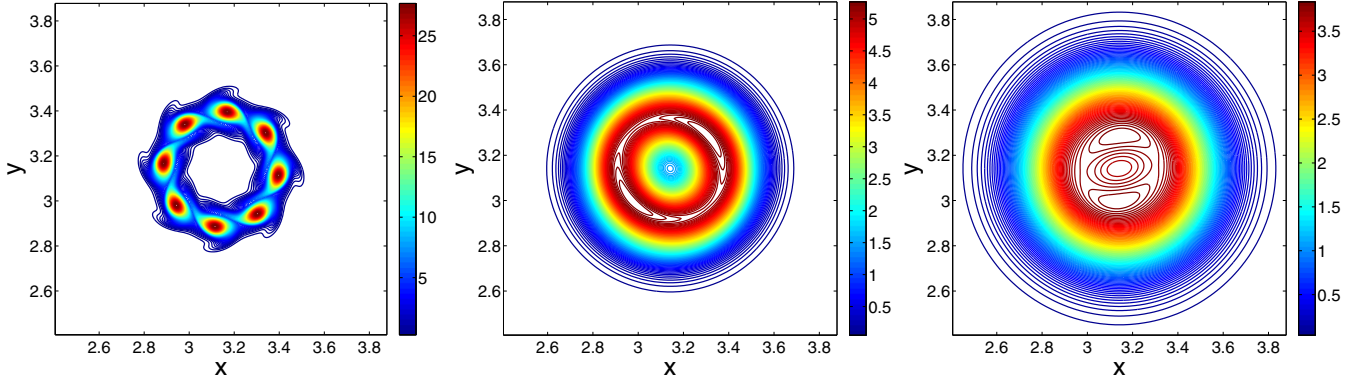


FIG. 12. Vorticity contours showing the viscous evolution of eight Gaussian vortices with $(a/d)_i = 0.1$ and $\text{Re}_\Gamma = 12\,000$. Left: $t = 0.1685$; center: $t = 10.0447$; right: $t = 25.0276$.

Figure 11(a) shows the distance d of the maximum vorticity point of each vortex from the center, as a function of time t , for different number of vortices, at $\text{Re}_\Gamma = 4000$. The length and time are nondimensionalized respectively by the initial separation d_i and the time scale T_Γ . A bend in the curve, where the coming together of the vortices slows down, is evident at $n = 3$ and $n = 4$. This bend corresponds to the formation of the annulus. Consequently, the convective stage is shorter in these cases. The convective stage completely disappears for six or more vortices. We have instead a new annular stage which is diffusive. Thus, the annular stage dominates the merger process as we increase the number of vortices, and spans the entire merger process for six and more vortices. This is a slow stage and effectively delays the merger. It can also be seen that as we increase the number of vortices, the process ceases to depend on the number of vortices. As we increase the number of vortices, there is a reduction in filament formation, which helps to slow down the approach of the vortices towards each other. In the simulations above, we have kept the initial Γ the same as we increase the number of vortices, and one may argue that in order to make a fair comparison between two different systems, it is the initial energy which has to be kept the same and not the initial circulation. We repeated all these simulations keeping the initial energy the same as we changed n , and we found that nothing changes qualitatively. The annular stage once again increasingly dominates the merger process as n increases, and effectively delays the merger. We note that holding (a/d) constant while increasing n makes the

n -vortex system look more and more like an annular vortex with perturbations. This will naturally bias the system towards forming an annulus, as is evident from Fig. 11(a).

Next we study the effect of changing Re_Γ on four-vortex merger; this is shown in Fig. 11(b). As expected, the duration of the first diffusive stage increases as the Reynolds increases. This is because the critical (a/d) is reached at a later time for lower relative viscosity. As is also true of the two-vortex case, the convective stage is almost independent of the Reynolds number. Most important, the final (annular) stage of merger is strongly dependent on the Reynolds number, with the duration scaling approximately linearly with the Reynolds number, suggesting that the annular stage is a diffusive stage.

We now look at what happens with eight and nine vortices. We choose $\text{Re}_\Gamma = 12\,000$ and $(a/d)_i = 0.1$. The results are shown in Fig. 12 for eight vortices and Fig. 13 for nine vortices. In both cases, the merger proceeds as discussed before in that the annulus forms and migrates inwards, but in the eight-vortex case, a small departure from axisymmetry, in the form of a tripolar vortex, is visible at late times. In the next section, we will contrast these results against eight- and nine-vortex dynamics at very high Reynolds number.

C. High Reynolds number multiple-vortex simulations

At higher Reynolds number, nonlinearity dictates the dynamics and the viscosity is not effective in making the vortices diffuse and merge. To capture the small scale structures

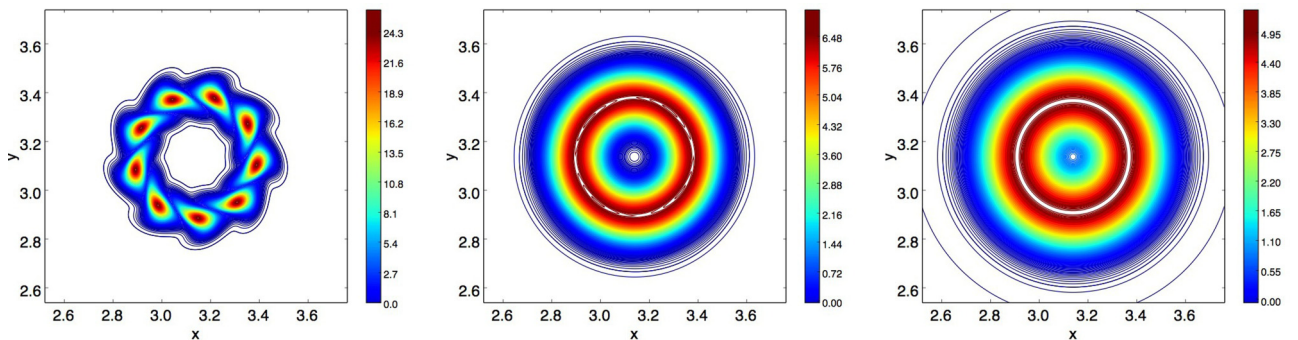


FIG. 13. Vorticity contours showing the viscous evolution of nine Gaussian vortices with $(a/d)_i = 0.1$ and $\text{Re}_\Gamma = 12\,000$ at times (in units of T_Γ): $t = 0.09$ (left panel), $t = 4.59$ (middle panel), and $t = 9.09$ (right panel).

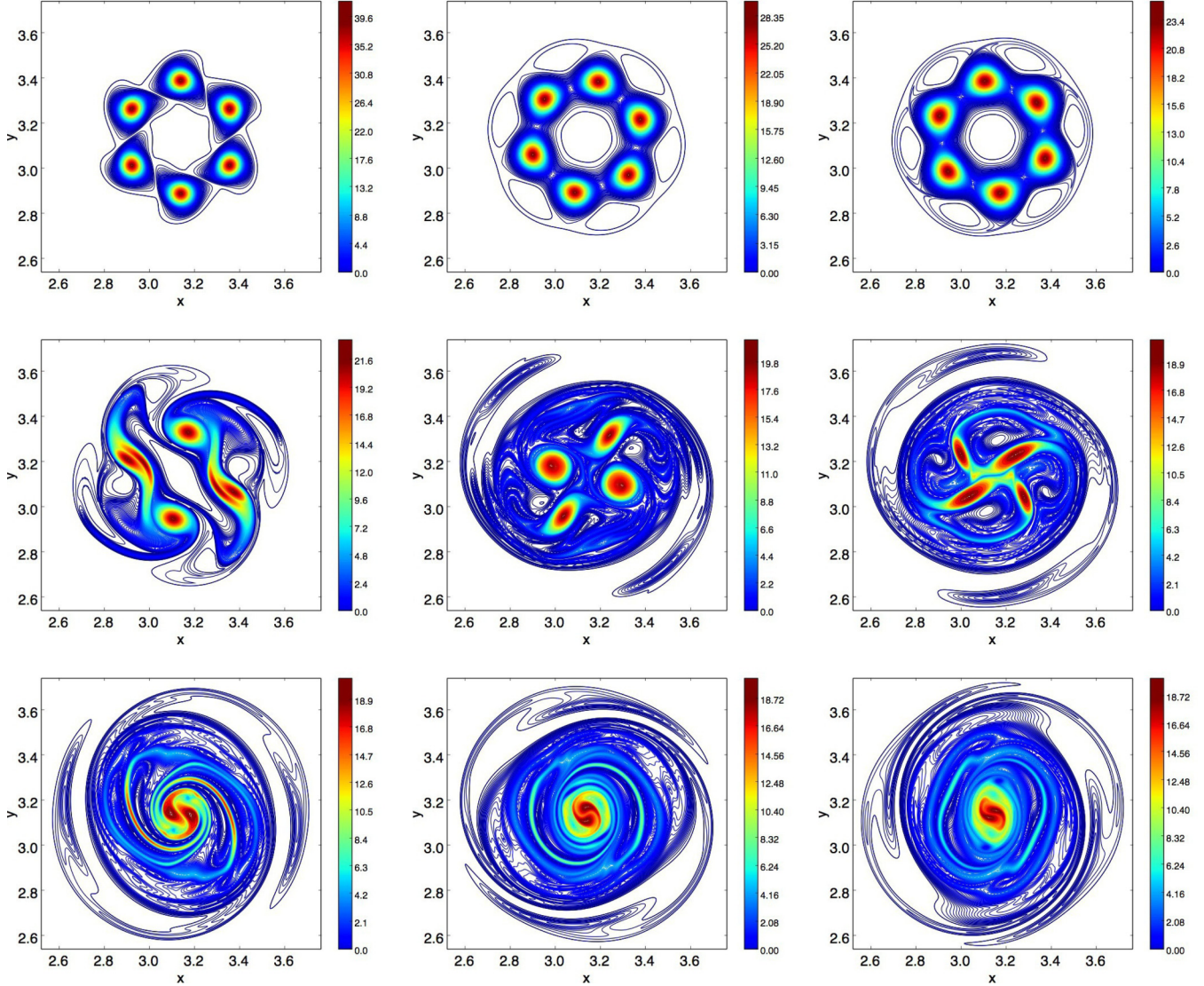


FIG. 14. Contours of vorticity showing the time evolution of a six-vortex configuration at $Re_T = 1.5 \times 10^5$. The different snapshots are at times (in units of $T_T \approx 0.74$) $t = 0.09$ (top left), $t = 6.42$ (top center), $t = 10.64$ (top right), $t = 12.75$ (middle left), $t = 14.86$ (middle center), $t = 15.71$ (middle right), $t = 16.13$ (bottom left), and $t = 16.55$ (bottom center), and $t = 16.89$ (bottom right).

that appear at high Reynolds number, we discretized the computational domain with 4096^2 collocation grid points. We find that the dynamics strongly depends on whether the number of vortices are even or odd (a feature not observed in linear stability).

1. Six-vortex merger, $Re_T = 1.5 \times 10^5$

We begin with an even number (six) of vortices arranged, as before, on the vertices of a regular polygon. The plot in Fig. 14 shows the time evolution of the vorticity contours during the merger process. Initially, the dynamics proceeds in a manner similar to that at moderate Reynolds number. The vortices start to rotate in the counterclockwise direction and try to form an annularlike structure. The annulus, however, is never formed. The six vortices undergo an asymmetric merger to first form four vortices, which are not identical. The two located diametrically opposite to each other, which came from

the merger events, are larger. This is followed by another pair of mergers to give two vortices, with a lot of fine filamentary structure in the neighborhood. Thus it is seen that reducing the viscosity reduces the propensity to form an annulus, and other, less regular dynamics intervenes.

2. Eight-vortex merger, $Re_T = 2 \times 10^5$

We now examine a multiple of four (i.e., eight) vortices on the vertices of a regular polygon, in Fig. 15. Now the first merger event is perfectly symmetric, with four pairwise mergers yielding four identical vortices. The perfect symmetry of this case is preserved through most of the later dynamics, whereas this is not possible in the six- and nine-vortex cases. Here the four-vortex structure continues to decay until, at a later stage, these vortices further merge to form a tripolar vortex.

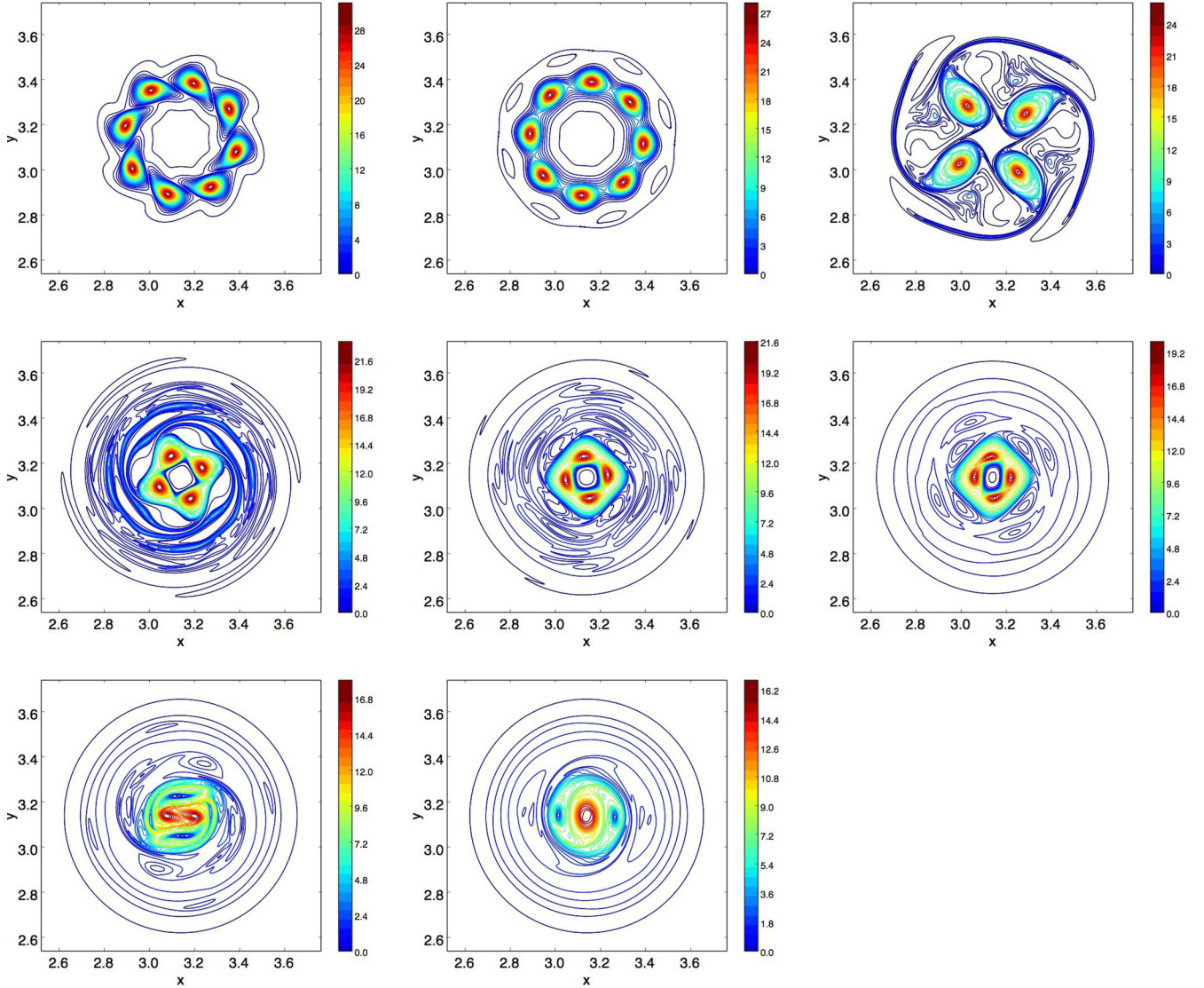


FIG. 15. Contours of vorticity showing the time evolution of an eight vortex configuration at $\text{Re}_\Gamma = 2 \times 10^5$. The different snapshots are at times (in units of T_Γ) $t = 0.09$ (top left), $t = 2.31$ (top center), $t = 4.52$ (top right), $t = 6.74$ (middle left), $t = 8.96$ (middle center), $t = 11.17$ (middle right), $t = 13.39$ (bottom left), and $t = 15.60$ (bottom right).

3. Nine-vortex merger, $\text{Re}_\Gamma = 2 \times 10^5$

The dynamics of an odd number (nine) of vortices arranged initially on the vertices of a regular polygon is very different from its even-number counterpart, since simple symmetric mergers can no longer take place. The plot in Fig. 16 shows the time evolution of the vorticity contours during the merger process. Initially the vortices start to rotate in the counter-clockwise direction and form an annular structure. However, because of an additional unpaired vortex this structure very quickly turns unstable and chaotic. We point out that, because of rapid mixing, the total time of merger is about half what is expected. At late times a single vortex at the center of the domain is formed.

D. Energy flux in vortex merger

We now discuss the merger of vortices by looking at the energy flux. The plot in Figs. 5 and 10 shows the evolution

of two ($\text{Re}_\Gamma = 4 \times 10^3$) and six ($\text{Re}_\Gamma = 1.5 \times 10^5$) vortex configurations. The corresponding plot for the energy flux $\Pi_k = \sum_{k'=k}^{N/2} \hat{\mathbf{v}}_{-k'} [\mathbf{v} \cdot \nabla \mathbf{v}]_{k'}$ is shown in Fig. 17. We find that energy flux remains negative, indicating transfer of energy from small to large scales, for the duration of the merger events. At intermediate times, as the filamentary structures start to develop around the vortices, we also observe a positive enstrophy cascade at high wave number.

IV. GENERALIZED LAMB-OSEEN VORTEX

We have seen that at moderate Reynolds numbers an annular vortex is formed. This vortex can be written down analytically as an exact solution of the axisymmetric Navier-Stokes equations. The analytical solution for the annular vortical structure from the viscous evolution of a circular vortex sheet was derived by [22]. We provide an alternative derivation in the Appendix. We call this solution the generalized Lamb-Oseen

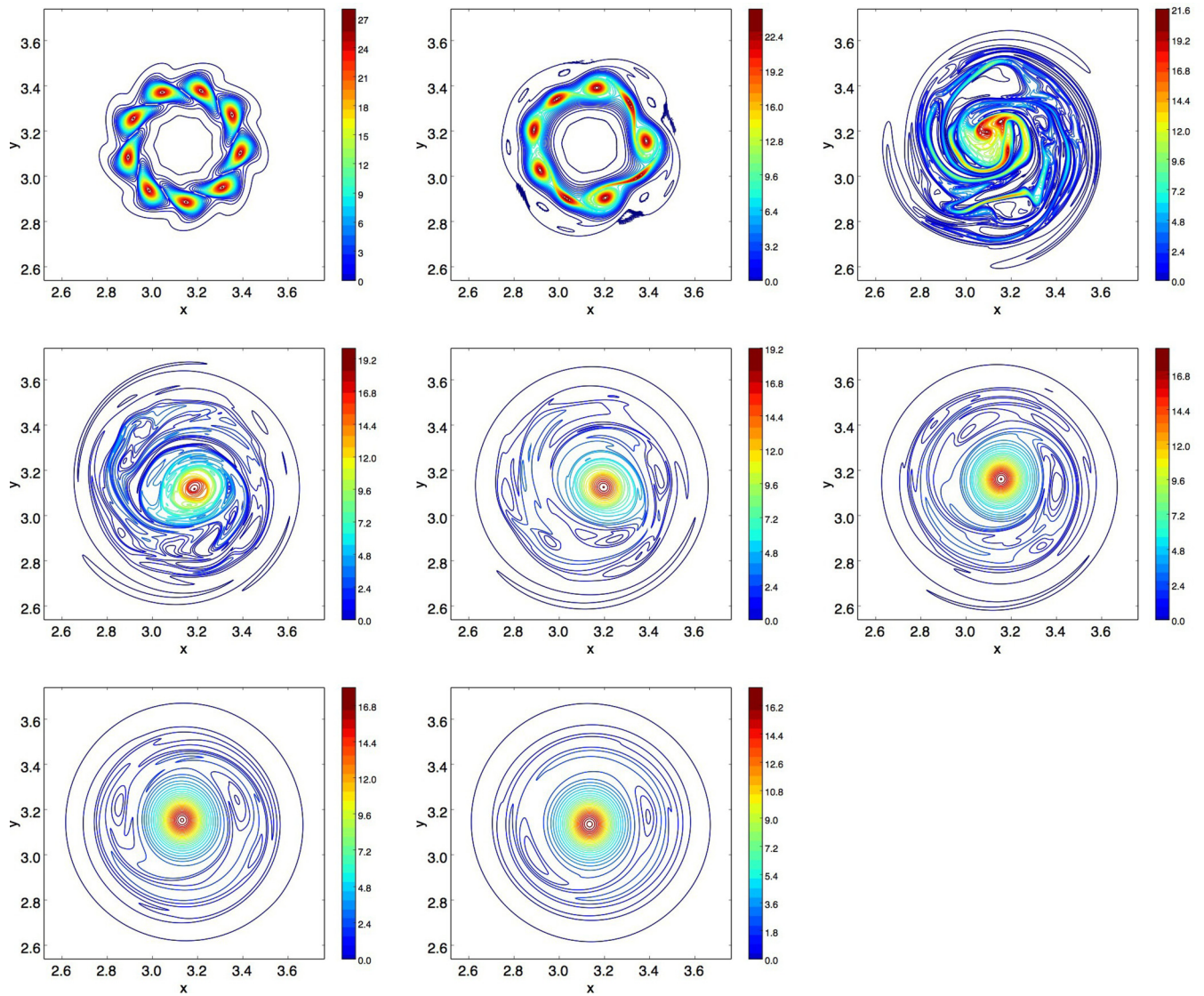


FIG. 16. Contours of vorticity showing the time evolution of a nine-vortex configuration at $\text{Re}_\Gamma = 2 \times 10^5$. The different snapshots are at times (in units of T_Γ) $t = 0.09$ (top left), $t = 2.34$ (top center), $t = 4.59$ (top right), $t = 6.85$ (middle left), $t = 9.09$ (middle center), $t = 11.35$ (middle right), $t = 13.59$ (bottom left), and $t = 15.85$ (bottom right).

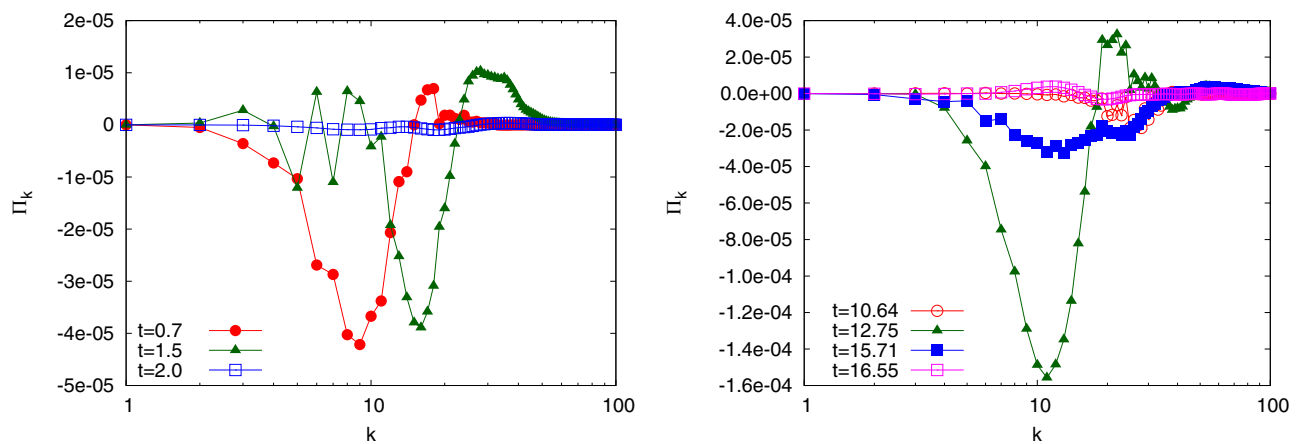


FIG. 17. Energy flux $\Pi(k)$ vs k for the two-vortex configuration (left) and the six-vortex configuration (right).

(GLO) vortex with vorticity concentrated within an annulus. Such a vortex results from the evolution of a cylindrical vortex sheet at a radius a with a circulation of Γ_o , given at $t = 0$ by

$$\omega(r, 0) = \frac{\Gamma_o}{2\pi r} \delta(r - a), \quad (6)$$

by the axisymmetric vorticity equation

$$\frac{\partial \omega}{\partial t} = \frac{\nu}{r} \frac{\partial}{\partial r} \left(r \frac{\partial \omega}{\partial r} \right). \quad (7)$$

The boundary conditions are symmetry at $r = 0$ and a vorticity-free far field. The generalized Lamb-Oseen vortex (see the Appendix) is then obtained as

$$\omega = \frac{\Gamma_o}{4\pi \nu t} e^{-[(a^2 + r^2)/4\nu t]} I_0 \left\{ \frac{ar}{2\nu t} \right\}, \quad (8)$$

where I_0 is the modified Bessel function of the first kind and zeroth order. Setting a to zero reduces the above to a standard Lamb-Oseen vortex. It is useful to note the nondimensional parameter $\nu t/a^2 = b^2$, which controls the profile of the GLO. Further, it is interesting to note that differentiating Eq. (8) with respect to time will yield additional solutions which satisfy the Navier-Stokes, including some that have net zero circulation.

At $t \rightarrow 0$, we may write the vorticity and, with some algebra, the location r_{\max} of the vorticity maximum, at leading order in t as

$$\omega = \frac{\Gamma_o}{4\pi^{3/2} a \sqrt{\nu t}} \exp \left[-\frac{(r - a)^2}{4\nu t} \right],$$

$$r_{\max} = a - \frac{1}{a} \nu t, \quad t \rightarrow 0. \quad (9)$$

Thus the vorticity maximum will move inwards purely due to diffusion, initially in a ballistic manner. Next, we may estimate the behavior as $r_{\max} \rightarrow 0$ by writing, at leading order,

$$r_{\max} = \frac{4\sqrt{2}\nu t}{a} \sqrt{\frac{a^2 - 4\nu t}{8\nu t - a^2}}. \quad (10)$$

The time taken for the vorticity maximum to reach the center is thus $a^2/(4\nu)$. Thus, for $\nu t/a^2 = b^2 < 0.25$, the GLO is an annular vortex sheet with the vorticity maxima away from the axis. For such a profile, a smaller b^2 corresponds to a thinner annular sheet. However, for $b^2 \geq 0.25$, we obtain a vortex with a vorticity maximum at the axis. Figure 18 contains plots for the evolution of r_{\max} and its early and late behavior, given by Eqs. (9) and (10).

In our simulations of merger above, in the cases when we arrived at an annular vortex, we found that the annular structure was, to a good approximation, the GLO vortex. In the following section we begin with a GLO vortex and perform numerical simulations with the method described above to check the analytical solution against the dynamics obtained numerically, and to study the stability of the annular structure.

Direct numerical simulations of the generalized Lamb-Oseen vortex

The linear and nonlinear stability of annular vortices has been well studied under the inviscid framework. Dritschel [12] considered an annular Rankine vortex with a fixed outer

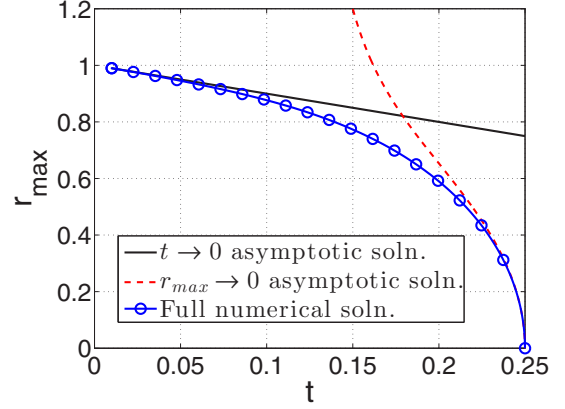


FIG. 18. Location of vorticity maximum r_{\max} . Time is nondimensionalized by a^2/ν .

radius and variable inner radius, and showed it to be linearly unstable when the inner radius exceeds half the outer radius. The cases which are linearly stable go through a steepening and sharpening of disturbance waves when nonlinearity is included, but reach a stable state nevertheless. The nonlinear instability leads to a breaking up into multiple vortices; an example of a five-vortex steady state emerging from an instability of the annular vortex is demonstrated.

The existing literature contains studies that report annular vortices becoming unstable to several modes of imposed perturbations. Reference [23] reports that initially thin annular vortices breakup in an $m = 5$ mode, forming mesovortices, and initially thick annular vortices breakup in an $m = 3$ mode. Reference [7] studies the stability of an annular vortex under imposed $m = 2$ perturbations and finds that wave interactions may dampen the growth of the perturbations. Reference [24] finds the existence of $m = 3$ and $m = 4$ modes in an actual hurricane.

We conduct a series of direct numerical simulations of the two-dimensional Navier-Stokes (NS) equations to study the evolution of the GLO vortex, and its stability to small perturbations of odd and even azimuthal wave number m . In what follows, the Reynolds number $\text{Re}_\Gamma \equiv \Gamma/\nu$ was varied by reducing the viscosity ν and keeping the circulation Γ fixed at a value of 6. To generate the GLO, we set the parameter $\nu_t \equiv \nu t = 0.001$, the distance from origin $a = 0.25$, and fix (π, π) as the center. The vertical y and horizontal x distances are measured from this center. We prescribe different values for the initial perturbation ϵ (see the remainder of Secs. IV and V). Radial perturbations are added by modifying the radius of a given vorticity to $r \rightarrow r + \epsilon \sin[m\theta]$, where m defines the azimuthal wave number of the perturbation, and θ is the azimuthal angle. The initial vortex structure for a GLO with a small perturbation is shown in Fig. 19. As it is unrealistic to scan the whole (m, Re_Γ) phase space with numerical simulations, we choose a few representative Reynolds numbers for four modes of disturbance, the even modes $m = 4$ and $m = 8$ and the odd modes $m = 5$ and $m = 9$.

To test the consistency of our numerics, we compare, in Fig. 20, numerical simulations of the dynamics of an annular vortex against the predicted evolution of the GLO from Eq. (8) both at a Reynolds number of 30 000. We expect the annulus

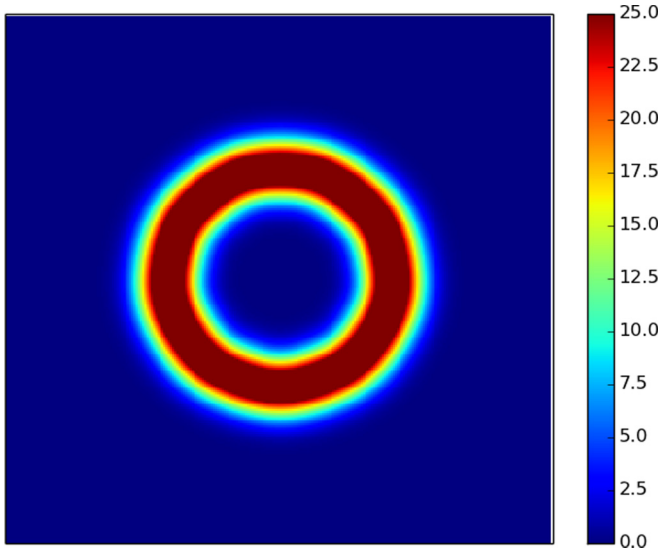


FIG. 19. Initial GLO vortex. The dark (red) regions indicate regions of intense vorticity whereas the light (blue) regions indicate regions of low vorticity. In all figures showing vorticity contours in the rest of the paper we have used the same color bar.

to be stable at this Reynolds number. These simulations were done with $\epsilon = 0.001$, and broadband noise. In this case, the perturbations do not grow visibly so we expect a good comparison with the theoretical GLO. The initial vortex in both is the same, and the width δ of the annular vortex in both cases is measured between the radial locations at which the vorticity drops to $1/e$ of its maximum value. Note that there are no fitting parameters. The widening with time of the annular region, as well as corresponding reduction in maximum vorticity of the numerical solution, agrees extremely well with the theoretical GLO. In the radial location of the maximum vorticity, the agreement between theory and simulations is very good at early times, but a departure from GLO behavior is seen at later times. The reason for this small departure could be small growths in the initial perturbations.

We next present, in Fig. 21, how the width of the annular vortex varies with time at a given azimuthal angle at a Reynolds number of 45 000, for an $m = 4$ perturbation of amplitude 10^{-6} of the reference vorticity. At this Reynolds number, oscillations in the width are evident at moderate times. The axisymmetric analytical solution is shown for comparison and is seen to be

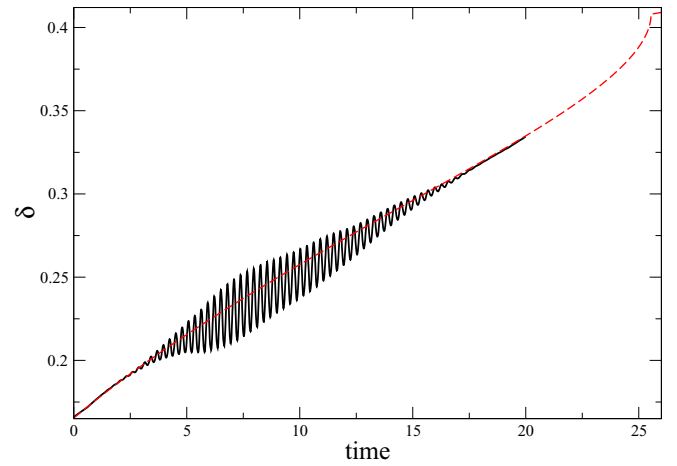


FIG. 21. Variation of the width of an annular vortex of $Re = 45\,000$ with time (solid black line). The initial condition contains an $m = 4$ perturbation of amplitude 10^{-6} of the reference vorticity. The analytical GLO evolution is shown by the (red) dashed line.

a good indicator of the growing width of the annular region. These oscillations grow for some time, and then decay.

Like the multiple-vortex systems above that behave differently for odd and even numbers of vortices, the annular vortex responds differently to perturbations of odd and even azimuthal wave numbers. We now discuss some cases to illustrate this.

1. Even mode radial perturbations: $m = 8$

The plot in Fig. 22 shows the evolution of a GLO vortex with an $m = 8$ mode perturbation. For Reynolds numbers $Re \leq 4.5 \times 10^4$, the vortex ring is stable to initial perturbations. On increasing the Reynolds number beyond $Re_r = 90\,000$ we observe that an initial instability sets in that makes a “four-vortex necklace” like structure. A similar structure had been seen in the early simulations of [8] (who used $Re = 10^5$ and an azimuthally broadband initial perturbation). For $Re = 9 \times 10^4$ the vortex necklace disappears at intermediate times, but another instability seems to appear at late times. On the other hand, for $Re \geq 1.35 \times 10^5$ the vortex necklace breaks into a tripolar vortex. Figure 23 shows the evolution of the width at a particular azimuthal angle of the annulus for $Re = 45\,000$ and perturbations of azimuthal wave number $m = 8$. It is seen that high frequency oscillations occur at early times, which decay

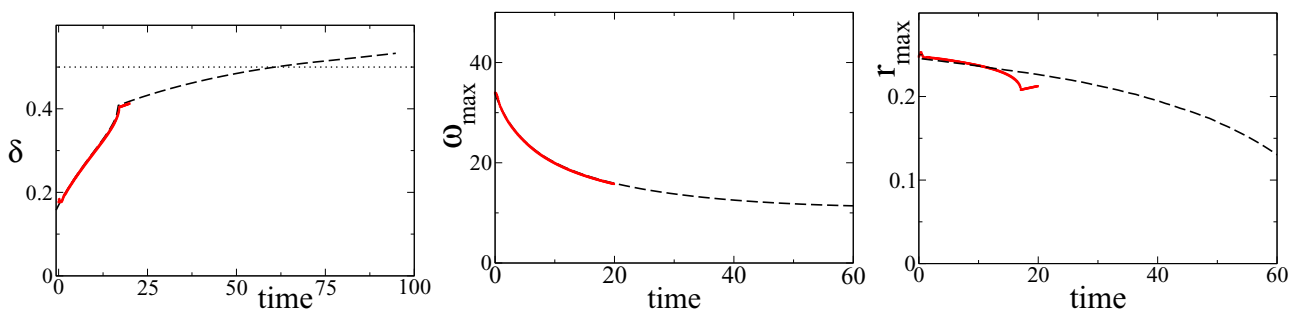


FIG. 20. Comparison of analytical evolution of the generalized Lamb-Oseen vortex with direct numerical simulations for $Re = 30\,000$. Left: Width of the annular region; center: maximum vorticity; right: location of the vorticity maximum. The (black) dashed lines are from the analytical expression whereas the solid (red) lines are from the simulations.

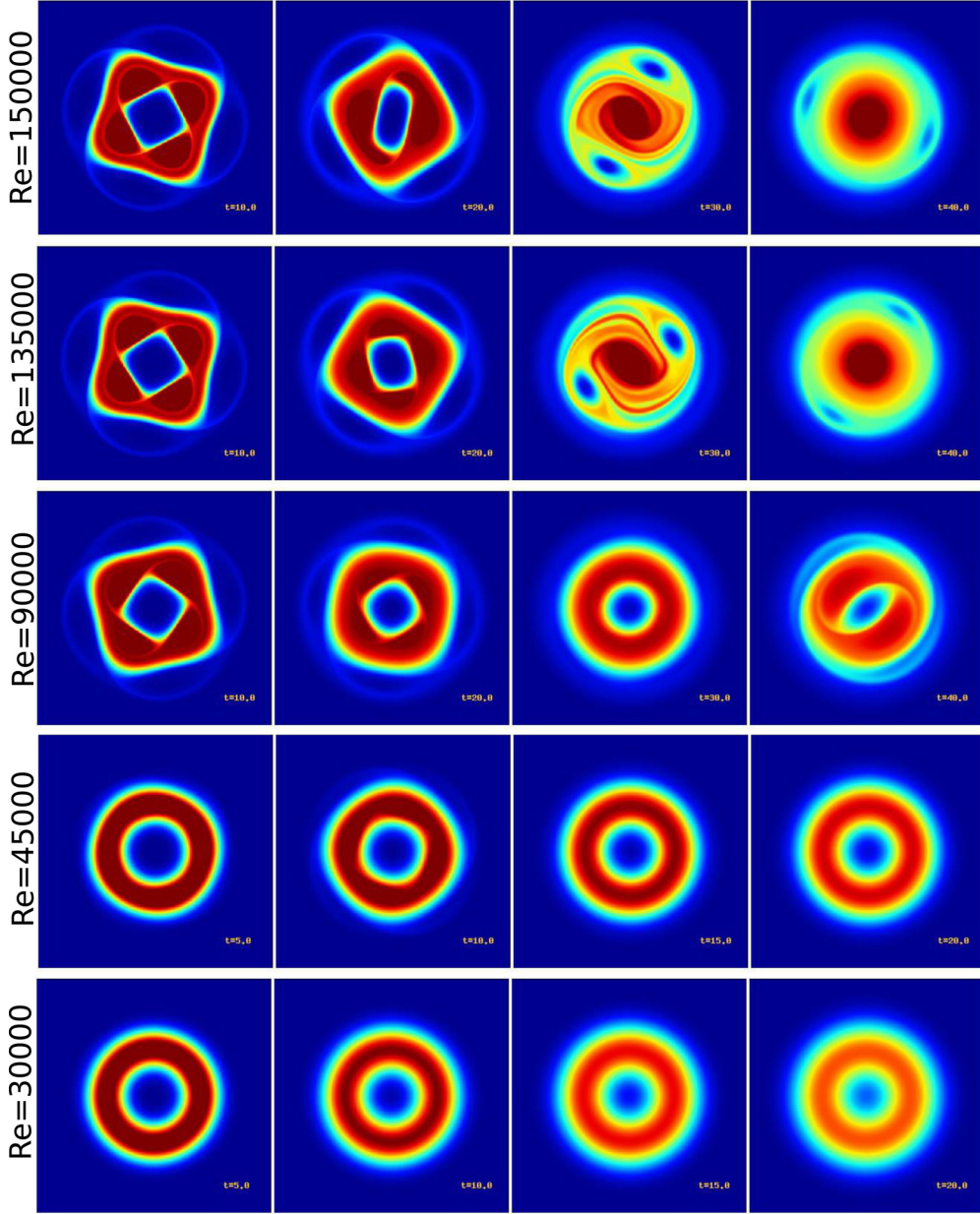


FIG. 22. Time evolution of the GLO annular vortex with an $m = 8$ mode perturbation for various Reynolds number (the same color bar as in Fig. 19 is used). For small Reynolds number the GLO is stable and the radial perturbations decay. At $\text{Re} = 9 \times 10^4$ instabilities start to appear. For even larger Reynolds numbers $\text{Re} = [1.35, 1.5] \times 10^5$, the GLO breaks into a four-vortex structure that later evolves into a tripolar vortex structure.

and give rise to low frequency oscillations at later times. The initial oscillations correspond to an $m = 8$ mode, as prescribed, whereas the low frequency oscillations are of $m = 4$, as is evident in Fig. 22 for this Reynolds number at a time of 10. Our provision of an $m = 8$ perturbation thus facilitates the growth of $m = 4$ perturbations. These in turn die down at this Reynolds number, as was seen in Fig. 22 at later times, and viscous processes take over.

2. Odd mode radial perturbation: $m = 5$ and 9

The plots in Figs. 24 and 25 show the time evolution of a GLO vortex with $m = 5$ and $m = 9$ mode perturbations at

different Reynolds number. At $\text{Re} = 30000$ and above, the $m = 9$ mode is linearly stable (see section V), but triggers the $m = 4$ mode which is unstable. We therefore see a four-vortex necklace. The $m = 5$ mode is linearly unstable above $\text{Re} = 30000$ and becomes turbulent without forming the four-vortex necklace.

A striking feature is that even the qualitative nature of evolution of instabilities is different for odd and even mode perturbations. For small values of Reynolds number the vortex ring is stable to odd-mode perturbations, as to even mode. On increasing the Reynolds number beyond $\text{Re} = 90000$, we do observe, with odd mode perturbations too, that an initial instability sets in that makes a “four-vortex necklace” like

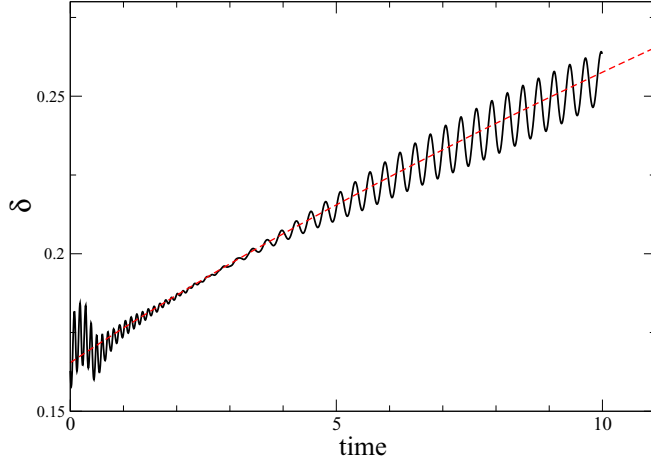


FIG. 23. Time variation of the width of an annular vortex at $Re = 45\,000$ with an initial $m = 8$ perturbation. Oscillations of this azimuthal wave number are seen at early times, which die down and give way to $m = 4$ perturbations visible at later times. The dashed (red) line is the analytical GLO evolution.

structure. At a later stage however, in contrast to the $m = 8$ mode perturbation, this structure breaks into filamentary structures and forms a turbulent patch. This feature stems from the fact that the vortex necklace is now less symmetric.

We next perform a linear stability analysis of the annular GLO vortex in order to better understand the results from our nonlinear simulations. We do not, however, expect the linear stability analysis to capture subtle differences between odd and even perturbation wave numbers.

V. LINEAR STABILITY ANALYSIS OF AN ANNULAR VORTEX

A thin cylindrical vortex sheet is linearly stable to axisymmetric perturbations in inviscid flow, as given by the condition for inviscid stability of Rayleigh [25], that $(rV)^2$ (V being the swirl velocity) should nowhere decrease as the radius r increases. Michalke and Timme [26] found such a vortex sheet to be unstable to nonaxisymmetric perturbations ($m \geq 1$, where m is the azimuthal wave number), so while Rayleigh's criterion is necessary and sufficient for axisymmetric

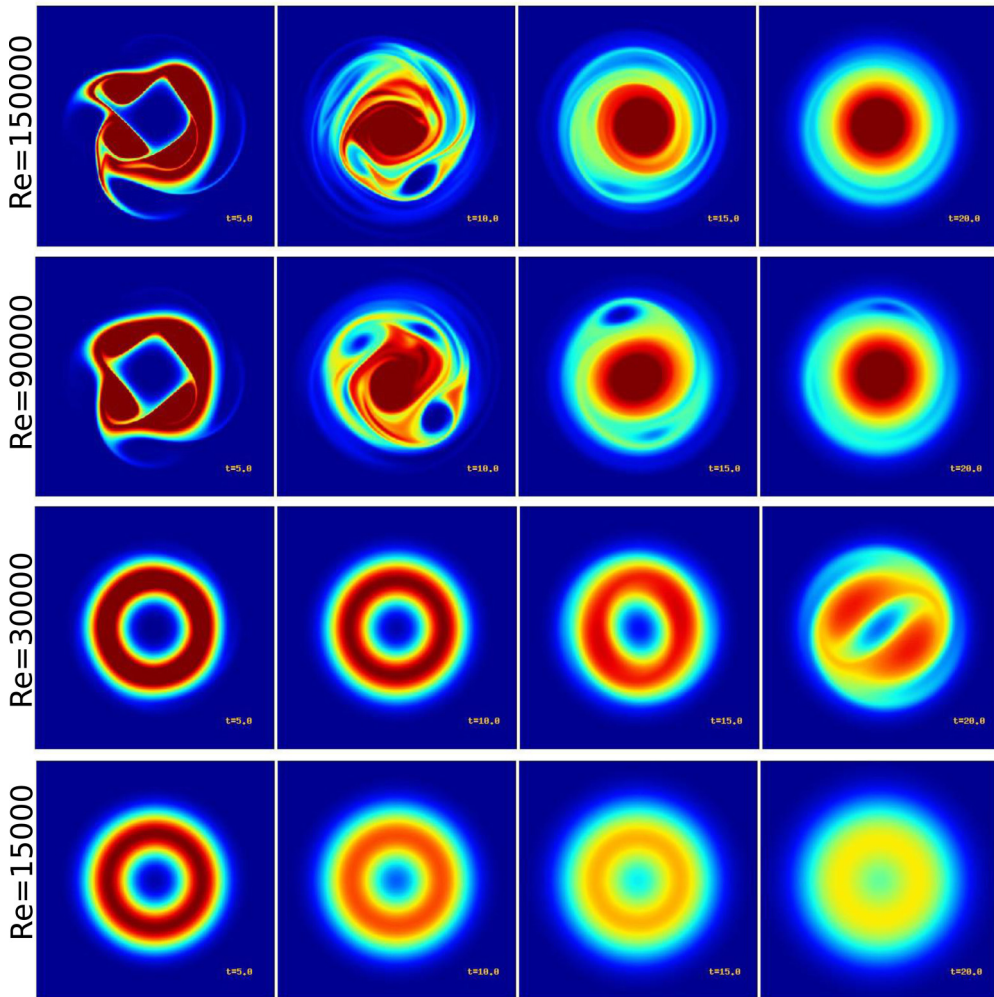


FIG. 24. Time evolution of the GLO annular vortex with an $m = 5$ mode perturbation for various Reynolds number (the same color bar as in Fig. 19 is used). For small Reynolds number the GLO is stable and the radial perturbations decay. However, at larger Reynolds number the GLO breaks into a four-vortex necklace. On further increasing the Reynolds number, this structure breaks up into a turbulent patch.

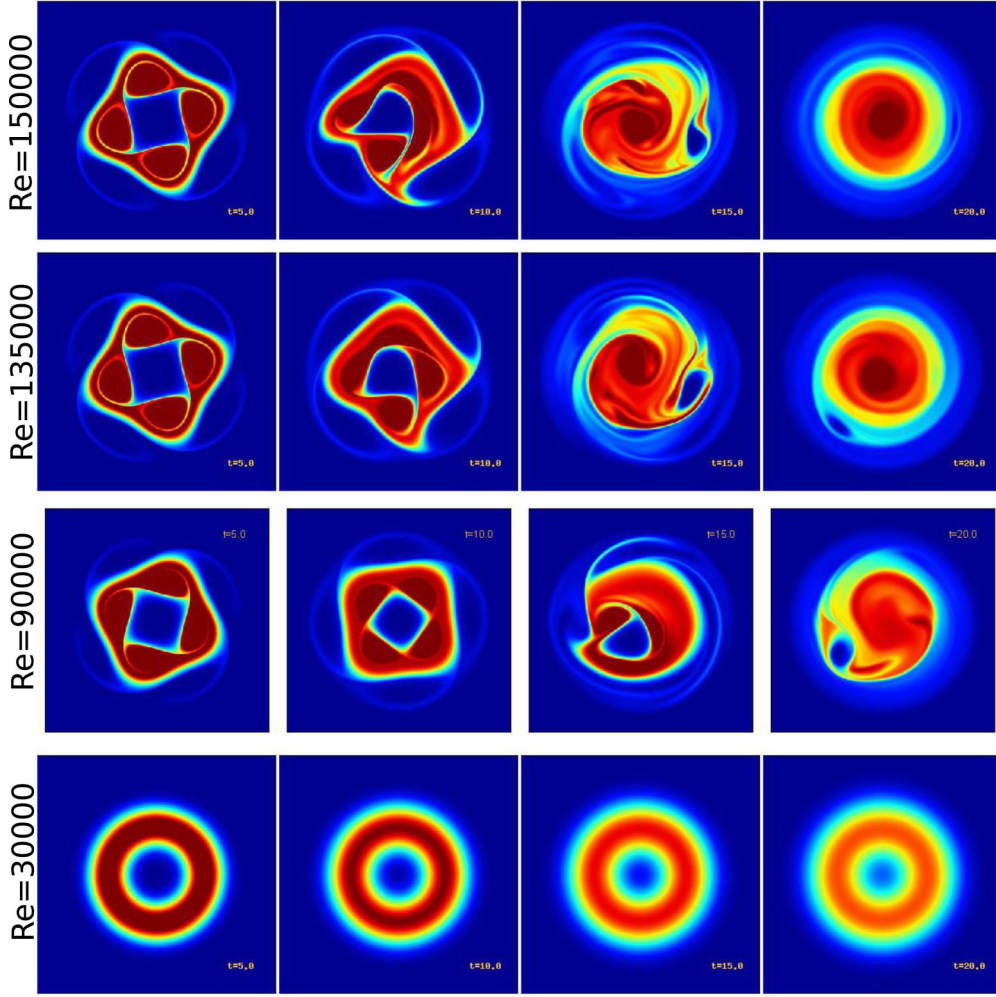


FIG. 25. Time evolution of the GLO annular vortex with an $m = 9$ mode perturbation for various Reynolds number (the same color bar as in Fig. 19 is used). For small Reynolds number the GLO is stable and the radial perturbations decay. However, at larger Reynolds number the GLO breaks into a four-vortex necklace. On further increasing the Reynolds number, this structure breaks up into a turbulent patch.

disturbances, for nonaxisymmetric disturbances it is necessary but not sufficient. Rotunno [27], Liebovich and Stewartson [28], Gent and McWilliams [29], Flierl [30], and Terwey and Montgomery [31] have studied different aspects of inviscid stability in two and three dimensions, and it is evident that a cylindrical vortex is inviscidly unstable to nonaxisymmetric perturbations. There are also several inviscid stability studies in the context of hurricanes and tornadoes. The authors of Ref. [8] report that their inviscid stability calculations show a maximum growth rate for the $m = 4$ mode. No studies, to our knowledge, have addressed the question of what happens in the viscous case, and so we conduct a viscous linear stability analysis.

The present problem is a time-varying one, and a linear stability study can only be conducted by making the frozen flow approximation. We use as our base flow a vorticity profile frozen at a given instant of time. This quasisteady approximation is the time analog of a parallel flow approximation made for spatially developing flows. The assumption here is that changes in the basic flow, caused because the annular vortex is growing in thickness due to diffusion, are far slower than the perturbation time scale. In other words,

during one oscillation of the perturbation wave, the change in thickness is so small that the GLO vortex can be taken to be constant during this time. The validity of the assumption for the present flow is estimated below by comparing actual perturbation time scales to the rate at which the GLO vortex thickness grows, and it will be seen that these time scales are separated by two orders of magnitude. The GLO vortex produces an entirely axisymmetric flow in which the nonlinear terms vanish. Perturbations imposed on the axisymmetric initial state bring the nonlinear terms into play. As the GLO vortex gets smoothed out by viscosity, we expect that the flow becomes less unstable to perturbations.

Following the standard procedure, we decompose the total motion into a background state and express the perturbations in their normal mode form, characterized by an azimuthal wave number m and a complex frequency f , as, e.g., for the azimuthal component of velocity

$$u_{\theta_{tot}} = U_{\theta}(r) + \hat{u}_{\theta}(r)e^{i(m\theta - ft)}. \quad (11)$$

Substituting such expressions into the two-dimensional incompressible continuity and Navier-Stokes equations in plane polar coordinates, neglecting nonlinear terms in the

perturbations, and eliminating pressure and \hat{u}_θ , we are left with an eigenvalue problem in the radial velocity component u_r :

$$A\hat{u}_r = fB\hat{u}_r. \quad (12)$$

The system is stable if the imaginary part of f , i.e., $f_i < 0$ and unstable if $f_i > 0$. A and B are linear differential operators given by

$$A = i\nu \left\{ r^2 D^4 + 6r D^3 + (5 - 2m^2) D^2 - \frac{(1 + 2m^2)D}{r} + \frac{(m^2 - 1)^2}{r^2} \right\} + m\Omega \{ r^2 D^2 + 3r D + (1 - m^2) \} - mr Z', \quad (13)$$

and

$$B = \{ r^2 D^2 + 3r D + (1 - m^2) \}, \quad (14)$$

where the operator $D \equiv d/dr$, angular velocity $\Omega = U_\theta/r$, and base flow vorticity $Z = U'_\theta + U_\theta/r$. Primes denote derivative with respect to r . The linear stability equations (12)–(14) are the same as Eq. (3.1) in [32], written for constant density. The boundary conditions depend on the mean profiles, which obey $U_\theta \sim r$ as $r \rightarrow 0$, $U_\theta \sim 1/r$ as $r \rightarrow \infty$. The boundary conditions are then deduced from the leading order terms of the Taylor series about $r = 0$ and $r \rightarrow \infty$, satisfying, for large Reynolds numbers,

$$\hat{u}_r \sim r^{|m|-1}, \text{ for } r \rightarrow 0, \text{ and } \hat{u}_r \sim r^{-|m|-1} \text{ as } r \rightarrow \infty. \quad (15)$$

A similar exercise for three-dimensional perturbations yields exponential, rather than algebraic, decay at large r . These boundary conditions were originally derived by Batchelor and Gill [33] in the form of compatibility relations, and were formalized later on by Lessen and Paillet [34] and Khorrami *et al.* [35].

We study the linear stability of the GLO vortex of Eq. (8). We have made detailed comparisons with a smoothed annular Rankine profile and get no qualitative difference in the answers. We solve the eigenvalue problem above using a

Chebyshev collocation technique. To specify a grid in the domain $[0, R_{\max}]$, and to cluster grid points into the vicinity of the annular vortex, we use a modified version of the algebraic stretching used by Khorrami *et al.* [35], given by

$$y = \frac{x(1 - \xi^3)}{q_1 + q_2\xi + (1 - q_2)\xi^3}, \quad q_1 = 1 + \frac{2x}{R_{\max}},$$

$$x = \frac{pR_{\max}}{R_{\max} - 2p}, \quad (16)$$

where ξ is the Chebyshev coordinate lying in $[-1, 1]$, p is the radius at which clustering is required, and q_2 is chosen to lie between 0.5 and 0.8. We have also used the exponential stretching of [36] and obtained the same answers. Our computational domain extends up to $R_{\max} = 1000$, and with the number of Chebyshev collocation points N of up to 1000.

Instability growth rates, as well as the azimuthal wave numbers, increase with increasing Reynolds number and, at high Reynolds numbers, are very similar to inviscid predictions. We discuss linear stability results for a Reynolds number of 45 000, which is high enough that disturbance growth is visible to the naked eye in the simulations, and small enough that at long times, viscous effects take over and the annulus returns to a GLO vortex. The circular frequency and growth rate of the most unstable perturbations from linear stability predictions, in the nondimensional units of the simulation, are given in Fig. 26.

Figure 26 also shows the existence of two $m = 2$ modes that are unstable. The slower-growing of the two is the same as that of [26]. A more detailed analysis of the faster growing $m = 2$ mode is done elsewhere, and will not be discussed further in the present study.

To compare the linear stability results with nonlinear dynamics, we return to the oscillations seen in Fig. 21. We subtract the width of the GLO vortex at every time, and plot the oscillations at early times in Fig. 27. Shown in the same figure is a best-fit curve, given by

$$\delta - \delta_{GLO} = 0.0008e^{2.5t} \sin[23t - 2.5]. \quad (17)$$

It is seen that the frequency of the oscillation is close to the value of 23.6 predicted by linear theory for $m = 4$. This

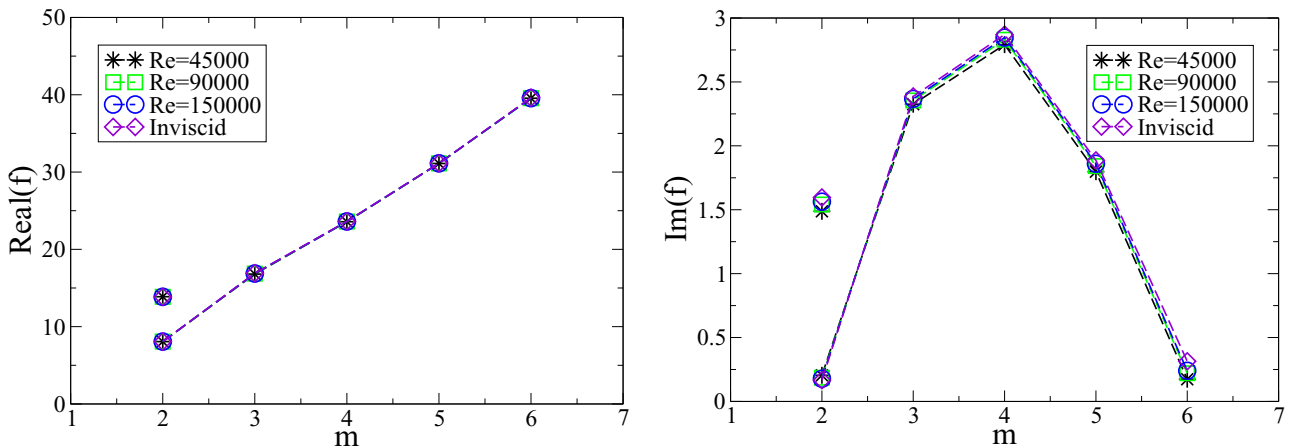


FIG. 26. Circular frequency (left) and growth rate (right) as a function of azimuthal wave number from the linear stability analysis. The $m = 4$ mode has the highest growth rate, and there are two unstable $m = 2$ modes (see text).

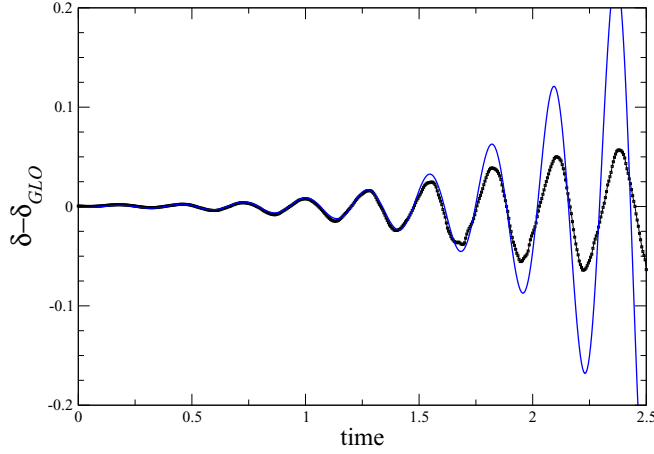


FIG. 27. A best fit of the oscillations seen at moderate times. The (black) filled squares are numerical simulations at $Re = 45\,000$, with an $m = 4$ perturbations of amplitude 10^{-3} in the vorticity. The (blue) line is a fit, given by Eq. (17).

frequency is maintained constant over a long time. However, we do not see any reasonable stretch of exponential growth, so nonlinearities are important throughout the evolution. We have performed $m = 4$ simulations with three amplitudes of initial perturbation, 10^{-6} , 10^{-3} , and 10^{-2} . All three show oscillations whose frequency is extremely well fitted by a value of 23. Exponential growth only occurs over short stretches of time in each case, and these best-fit growth rates are different, at 1.75, 2.5, and 3.5 respectively. These growth rates compare well with the linear stability growth rate of 2.8. The simulation of [8] was for a Reynolds number of 10^5 , and although they used only 512^2 grid points at this high Reynolds number, the growth rate they report is also comparable. In Fig. 23, we find initial oscillations of azimuthal wave number 8 whose frequency is very close to the value of 58.17 obtained by linear stability, but

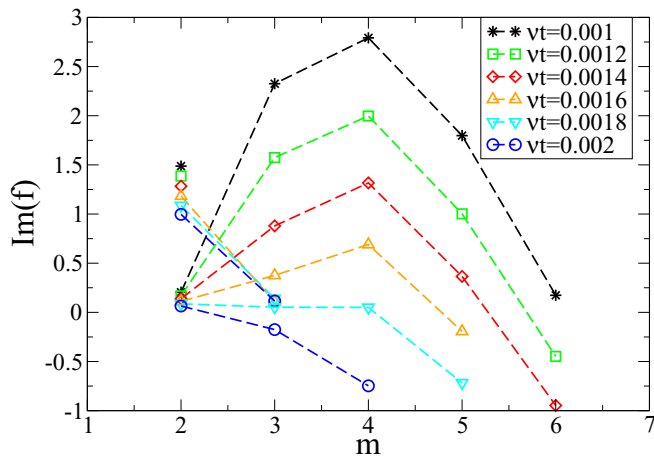


FIG. 28. Growth rate as a function of azimuthal wave number for varying initial δ or $b^2 = \nu t/a^2$ from the linear stability analysis for a Reynolds number of 45 000. $\nu t = 0.001$ corresponds to our initial profile or a simulation time of zero. $\nu t = 0.002$ corresponds to a simulation time of 7.5.

no evidence of exponential growth. The $m = 4$ oscillations at later time are of frequency close to 24. Such behavior is not uncommon in shear flows, with the frequency predicted by linear stability studies being quite prominent in the dynamics even after nonlinearities have become dominant (see Fig. 28).

We return to re-examine the frozen-flow assumption by the typical case of $m = 4$ seen above. Equation (17) gives the perturbation time scale as 1.7^{-1} , and it may be seen from Fig. 21 that during the time period of one oscillation of the perturbation, the analytical base state of the annular GLO vortex, shown by the dashed line, grows in thickness by around 1%. Thus we see that the time scales of the base state and the perturbation are vastly separated and the frozen-flow approximation is valid.

VI. DISCUSSION AND CONCLUSION

To summarize, we first study the viscous dynamics of $n \geq 3$ vortices placed at the vertices of a regular polygon. In inviscid flow, arrangements of patches of uniform vorticity are known to behave similarly to point vortices as long as their radii are smaller than a critical threshold. Above this threshold, the vortices deform significantly and tend toward merger. The role of viscosity in this initial stage of the dynamics is to grow the radii of the vortices past the critical radii. At moderate Reynolds number, the vortices align themselves into a long-lived annular structure. The annular vortex may be described analytically as a generalized Lamb-Oseen vortex, which diffuses slowly inwards to form a single Gaussian vortex at long times. The annular stage dominates the merger process more as the number of vortices increases, effectively delaying the merger. At high Reynolds numbers, a single vortex at the center is attained at large times, but there is no annular structure formation. Remarkably, and the behavior for odd and even number of vortices is qualitatively different. When n is even, the merger process at high Reynolds numbers is characterized by vortex pairing events rather than annulus formation. The option of complete vortex pairing is not available when n is odd, and a breakdown into chaotic motion is seen. In a much shorter time than when n is even, a single central vortex is formed. As expected, the merger events cause energy to first cascade to larger length scales, whereas the formation of filamentary structures causes a cascade of energy to smaller scales.

We then study the annular vortex in some detail, performing numerical simulations and (viscous) stability analysis. The time evolution of our numerical simulations of the annular vortex agrees extremely well with our generalized Lamb-Oseen solution for low Reynolds numbers. Our numerical simulations show that the annular vortex is stable to imposed perturbations at $Re = 45\,000$ and below, while instabilities clearly influence dynamics at $Re = 90\,000$ and above. The nonlinear evolution of even and odd mode perturbations is strikingly different. Again the odd mode perturbations result in a more chaotic flow, and collapse to a single vortex at much shorter times, whereas even modes proceed via reduction of wave number to effect a large slow down of the inverse cascade process.

This work, we hope, will motivate experimenters and simulators of two-dimensional turbulence to evaluate the contributions to the inverse cascade of multiple vortex interactions.

APPENDIX

Taking the Laplace transform in time of Eqs. (7) and using Eq. (6), we get

$$\frac{d^2\hat{\omega}}{dr^2} + \frac{1}{r} \frac{d\hat{\omega}}{dr} - \frac{s\hat{\omega}}{v} = -\frac{\omega(r,0)}{v} = f(r), \quad (\text{A1})$$

where $\hat{\omega}$ is the Laplace transform of ω . The homogeneous part is a modified Bessel equation in the variable $r\sqrt{\frac{s}{v}}$, whose solution is

$$\hat{\omega}_h = c_1 I_0\left(r\sqrt{\frac{s}{v}}\right) + c_2 K_0\left(r\sqrt{\frac{s}{v}}\right), \quad (\text{A2})$$

where I_0 and K_0 are modified Bessels functions of the first and second kind respectively [37]. The particular solution is obtained by variation of parameters, as

$$\hat{\omega}_p = I_0\left(r\sqrt{\frac{s}{v}}\right) \int_0^r r' f(r') K_0\left(r'\sqrt{\frac{s}{v}}\right) dr'$$

$$- K_0\left(r\sqrt{\frac{s}{v}}\right) \int_0^r r' f(r') I_0\left(r'\sqrt{\frac{s}{v}}\right) dr', \quad (\text{A3})$$

The complete solution $\hat{\omega} = \hat{\omega}_h + \hat{\omega}_p$. Applying the boundary conditions, which require that $\hat{\omega}$ be finite at $r = 0$, and that $\hat{\omega} \rightarrow 0$ as $r \rightarrow \infty$, and remembering that K_0 and I_0 diverge respectively as $r \rightarrow 0$ and ∞ , we get

$$\hat{\omega} = \begin{cases} \frac{\Gamma_0}{2\pi v} I_0\left(r\sqrt{\frac{s}{v}}\right) K_0\left(a\sqrt{\frac{s}{v}}\right) & \text{for } r \leq a, \\ \frac{\Gamma_0}{2\pi v} I_0\left(a\sqrt{\frac{s}{v}}\right) K_0\left(r\sqrt{\frac{s}{v}}\right) & \text{for } r > a. \end{cases} \quad (\text{A4})$$

It can be seen that the symmetry condition [Eq. (A1)] is automatically satisfied. Taking the inverse Laplace transform, and using the standard result from Erdélyi [38],

$$\begin{aligned} L^{-1}\{K_n[\sqrt{s}(\sqrt{\alpha} + \sqrt{\beta})]I_n[\sqrt{s}(\sqrt{\alpha} - \sqrt{\beta})]\} \\ = \frac{1}{2t} e^{-[(\alpha+\beta)/2t]} I_n\left\{\frac{\alpha + \beta}{2t}\right\}, \end{aligned} \quad (\text{A5})$$

we get Eq. (8).

-
- [1] A. Hassan, *J. Math. Phys.* **48**, 065401 (2007).
 - [2] G. Boffetta and R. E. Ecke, *Annu. Rev. Fluid Mech.* **44**, 427 (2012).
 - [3] R. Pandit, P. Perlekar, and S. S. Ray, *Pramana* **73**, 157 (2009).
 - [4] S. G. Danilov and D. Gurarie, *Phys. Usp.* **43**, 863 (2000).
 - [5] M. V. Melander, N. J. Zabusky, and J. C. McWilliams, *J. Fluid Mech.* **195**, 303 (1988).
 - [6] C. Cerretelli and C. H. K. Williamson, *J. Fluid Mech.* **493**, 219 (2003).
 - [7] K. Menelaou, M. K. Yau, and Y. Martinez, *J. Atmos. Sci.* **70**, 559 (2013).
 - [8] W. H. Schubert, T. M. Montgomery, R. T. Taft, T. A. Guinn, S. R. Fulton, J. P. Kossin, and J. P. Edwards, *J. Atmos. Sci.* **56**, 1197 (1999).
 - [9] D. G. Dritschel, *J. Fluid Mech.* **157**, 95 (1985).
 - [10] J. J. Thomson, *A Treatise on the Motion of Vortex Rings* (MacMillan, New York, 1883).
 - [11] T. H. Havelock, *Philos. Mag.* **11**, 617 (1932).
 - [12] D. G. Dritschel, *J. Fluid Mech.* **172**, 157 (1986).
 - [13] C. Pozrikidis, *Introduction to Theoretical and Computational Fluid Dynamics* (Oxford University Press, New York, 2011).
 - [14] C. Canuto, M. Y. Hussaini, A. Quateroni, and T. A. Zang, *Spectral Methods: Fundamentals in Single Domains* (Springer, New York, 2006).
 - [15] P. Perlekar, S. S. Ray, D. Mitra, and R. Pandit, *Phys. Rev. Lett.* **106**, 054501 (2011).
 - [16] P. Meunier, U. Ehrenstein, T. Leweke, and M. Rossi, *Phys. Fluids* **14**, 2757 (2002).
 - [17] P. Meunier and T. Leweke, *J. Fluid Mech.* **533**, 125 (2005).
 - [18] O. U. Velasco Fuentes, *Dyn. Atmos. Oceans* **40**, 23 (2005).
 - [19] M.-J. Huang, *Phys. Fluids* **17**, 074105 (2005).
 - [20] L. K. Brandt and K. K. Nomura, *Phys. Fluids* **18**, 051701 (2006).
 - [21] L. K. Brandt and K. K. Nomura, *J. Fluid Mech.* **592**, 413 (2007).
 - [22] J. P. Kossin and W. H. Schubert, *J. Atmos. Sci.* **60**, 586 (2003).
 - [23] E. A. Hendricks and W. H. Schubert, *J. Adv. Model. Earth Syst.* **2**, 19 (2010).
 - [24] K. Menelaou, M. K. Yau, and Y. Martinez, *J. Atmos. Sci.* **70**, 3839 (2013).
 - [25] J. W. S. Rayleigh, *Proc. R. Soc. London, Ser. A* **93**, 148 (1917).
 - [26] A. Michalke and A. Timme, *J. Fluid Mech.* **29**, 647 (1967).
 - [27] R. Rotunno, *J. Fluid Mech.* **87**, 761 (1978).
 - [28] S. Leibovich and K. Stewartson, *J. Fluid Mech.* **126**, 335 (1983).
 - [29] P. R. Gent and J. C. McWilliams, *Geophys. Astrophys. Fluid Dyn.* **35**, 209 (1986).
 - [30] G. R. Flierl, *J. Fluid Mech.* **197**, 349 (1988).
 - [31] W. D. Tervey and M. T. Montgomery, *J. Atmos. Sci.* **59**, 2421 (2002).
 - [32] H. D. Dixit and R. Govindarajan, *J. Fluid Mech.* **646**, 415 (2010).
 - [33] G. K. Batchelor and A. E. Gill, *J. Fluid Mech.* **14**, 529 (1962).
 - [34] M. Lessen and F. Paillet, *J. Fluid Mech.* **65**, 769 (1974).
 - [35] M. R. Khorrami, M. R. Malik, and R. L. Ash, *J. Comput. Phys.* **81**, 206 (1989).
 - [36] R. Govindarajan, *Intl. J. Multiphase Flow* **30**, 1177 (2004).
 - [37] M. Abramowitz and I. A. Stegun, *Handbook of Mathematical Functions* (Dover, New York, 1965).
 - [38] A. Erdélyi, *Tables of Integral Transforms* (McGraw-Hill, New York, 1954).